Editors' Suggestion

Proposal for resolving quantized Landau orbits via elastic XUV scattering

Sabrina Meyer,[1,*] Joris Sturm,[1] Christina Schröder,[1] Stephen Hughes,[2] Andreas Knorr,[1] and Lara Greten[1,2,†]
[1]*Nichtlineare Optik und Quantenelektronik, Institut für Physik und Astronomie, Technische Universität Berlin, Berlin, Germany*
[2]*Department of Physics, Engineering Physics and Astronomy, Queen's University, Kingston, Ontario, Canada*

(Received 18 November 2025; accepted 23 March 2026; published 21 April 2026)

Electrons in a two-dimensional electron gas under a strong perpendicular magnetic field undergo cyclotron motion, whose quantization yields discrete Landau levels and quantized Larmor radii. The magnetic length—the Larmor radius of the smallest Landau orbit—is only tens of nanometers for fields of a few tesla. We propose a method to probe the spatial structure of Landau orbits via scattering with extreme ultraviolet radiation, whose wavelength naturally matches this scale. Starting from a microscopic Hamiltonian, we derive the far-field spectrum emitted by the optically induced current density. The Landau orbit contributions in the spectrum are suppressed due to scattering at the sample geometry. However, normalizing to the zero-magnetic-field reference defines a Landau-level scattering spectrum that isolates Landau orbit information from the full spectrum. A projection onto Laguerre polynomials allows for reconstructing the probability density distributions of individual Landau-level wave functions, featuring radial maxima at the quantized Larmor radii. This way, we propose an experimental method to determine details of the Landau orbits.

DOI: 10.1103/hq91-75kb

I. INTRODUCTION

A two-dimensional electron gas (2DEG), e.g., electrons confined to a quantum well [1], subject to a strong perpendicular, homogeneous magnetic field, gives rise to a variety of unique quantum phenomena, such as the integer [2] and fractional quantum Hall effect [3], the Shubnikov–de Haas effect [4], or Weiss oscillations [5] in the presence of an additional periodic potential. The common origin of these effects is the quantization of the electronic cyclotron motion into discrete Landau levels (LLs) [6,7], the quantum analog of classical cyclotron orbits.

In the symmetric gauge, where the vector potential is $\mathbf{A}_B(\mathbf{r}) = \frac{1}{2}\mathbf{B} \times \mathbf{r}$, each state $|\varphi_{\ell,m}\rangle$ with quantum numbers ℓ, m, describes a Landau orbit with Larmor radius

$$r_c = l_B\sqrt{2\ell + 1}, \tag{1}$$

centered around a guiding center with radial distance from the origin [8]

$$r_g = l_B\sqrt{2m + 1}. \tag{2}$$

Both the Larmor radius r_c [Eq. (1)] and guiding center r_g [Eq. (2)] scale linearly with the magnetic length [9]

$$l_B = \sqrt{\frac{\hbar}{eB}}. \tag{3}$$

Figure 1 shows an illustration of the spatial distribution of Landau orbits.

For magnetic field strengths of a few tesla, the characteristic length scale l_B of Landau orbits is on the order of tens of nanometers. Probing their spatial structure therefore requires techniques with correspondingly high spatial resolution. Previously, this has been achieved via scanning tunneling spectroscopy, e.g., see Ref. [10], observing characteristic radial nodes of higher Landau orbits from minima in the Fourier transform of the local density of states. Here, we propose an *optical probe* utilizing elastic scattering of extreme ultraviolet (XUV) radiation to obtain spatial information of Landau orbits in a quantized 2DEG ground state.

Light scattering at Landau levels has already been extensively discussed in the terahertz-frequency regime, featuring energies on the order of inter-LL transitions [11]; previous works studied inelastic light scattering by Landau-quantized 2DEGs, i.e., Raman scattering [12–15] and resonant inelastic light scattering [16–19], observing changes in LL energy quantum number ℓ up to $\Delta\ell = 7$ [20]. Elastic light scattering is typically discussed within the framework of resonant Rayleigh scattering [21–23], which was shown to be an effective probe of the spin degree of freedom [19,24,25].

In contrast, less literature is available on XUV scattering at LLs, featuring wavelengths on the order of the magnetic length l_B. In this context, Ref. [26] predicted a decrease of the scattering-induced spectral broadening of LLs in an intense high-frequency electromagnetic field, however, without extracting any spatial information.

Our main aim is to connect the spatial structure of Landau orbits (see Fig. 1), with elastic XUV scattering in the linear regime, i.e., scattering of weak high-frequency fields. Figure 2 illustrates the proposed measurement. A circular 2DEG of area $A = \pi R^2$ with radius R is exposed to a static

*Contact author: meyer@tu-berlin.de
†Contact author: lara.greten@queensu.ca

Published by the American Physical Society under the terms of the Creative Commons Attribution 4.0 International license. Further distribution of this work must maintain attribution to the author(s) and the published article's title, journal citation, and DOI.

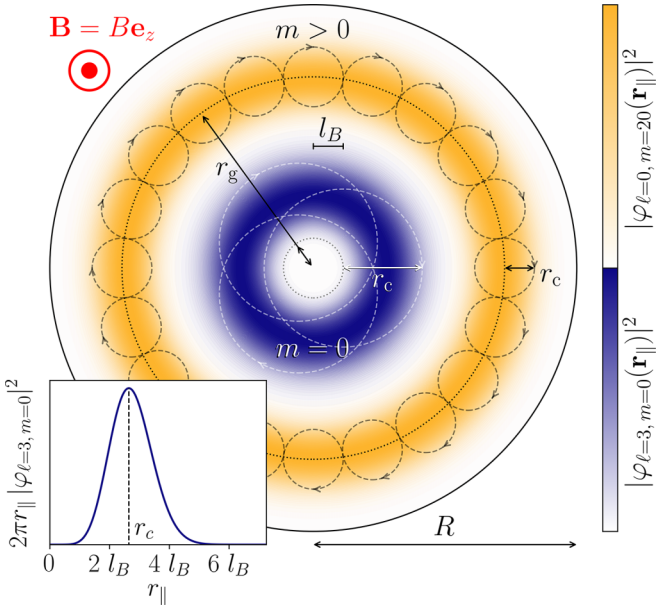


FIG. 1. Schematic spatial distribution of Landau orbits in a circular 2DEG of radius R (solid circle; not to scale for visual clarity). In symmetric gauge, each Landau state $|\varphi_{\ell,m}\rangle$ describes Landau orbits (represented by dashed circles) with Larmor radius $r_c(\ell)$ [Eq. (1)] around a guiding center (dotted circles) with absolute value $r_g(m)$ [Eq. (2)]. The magnetic length l_B [Eq. (3)] is the lower bound for both Larmor radius r_c, and guiding center r_g. The probability density $|\varphi_{\ell,m}(\mathbf{r}_\parallel)|^2$ [cf. Eq. (9)] is exemplarily shown in blue (orange) for $m = 0$ ($\ell = 0$) such that $r_g = l_B$ ($r_c = l_B$). The inset shows the angle-integrated probability density $2\pi r_\parallel |\varphi_{\ell=3,m=0}|^2$, over the radius $r_\parallel$ in units of the magnetic length l_B, featuring a maximum at the corresponding Larmor radius $r_c(\ell = 3)$, which is indicated by a dashed line.

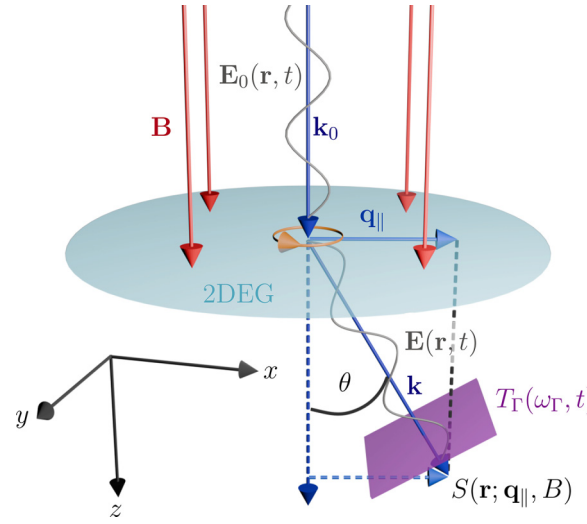


FIG. 2. Setup. Electrons in a 2DEG are quantized into LLs—exemplarily depicted as an orange cyclotron motion—in a perpendicular static magnetic field $\mathbf{B} = B\mathbf{e}_z$. The incident optical field $\mathbf{E}_0(\mathbf{r}, t) = -\frac{\partial}{\partial t}\mathbf{A}_0(\mathbf{r}, t)$ with wave vector $\mathbf{k}_0 = \frac{\omega_0}{c}\mathbf{e}_z$ is scattered by the LL states into the scattered electric field $\mathbf{E}(\mathbf{r}, t)$ [Eq. (16)], with propagation direction of the wave vector $\mathbf{k} = \frac{\omega}{c}\mathbf{e}_r$. For elastic scattering, the magnitude $q_\parallel = \frac{\omega_0}{c}\sin\theta$ of the in-plane component of the scattering vector $\mathbf{q} = \mathbf{k} - \mathbf{k}_0$ depends on the incident frequency ω_0 and the detection angle θ. A detector at position $\mathbf{r}$ measures the elastic steady-state scattering spectrum $S(\mathbf{r}; \mathbf{q}_\parallel, B)$ [Eq. (34)] behind a spectral bandpass filter $T_\Gamma(\omega_\Gamma, t)$ [Eq. (19)].

perpendicular magnetic field $\mathbf{B} = B\mathbf{e}_z$. Incident radiation with perpendicular wave vector $\mathbf{k}_0$ is scattered to the direction $\mathbf{k}$ at an angle θ. The corresponding in-plane scattering vector is given by $\mathbf{q}_\parallel$. For normal incidence $\mathbf{k}_0 \perp \mathbf{q}_\parallel$, the magnitude of the in-plane scattering vector $q_\parallel$ relates to the scattering angle θ via

$$q_\parallel = |\mathbf{k}_0| \sin\theta. \tag{4}$$

The scattered field passes through a frequency-selective bandpass filter T_Γ with central frequency ω_Γ and spectral width Γ, before the dark-field (excluding the incident beam) scattering spectrum S is detected. Figure 2 schematically shows the transmission; however, the considered effect could also be observable in reflection. Both measurement approaches are experimentally accessible using surface 2DEGs, e.g., doped semiconductors [10,27].

Note that we focus on the spatial structure of Landau orbits directly imprinted by the magnetic field, but disregard additional effects, such as electron-electron Coulomb interactions or spin [28]. Therefore, the results are not applicable for exotic, topological states, i.e., filling factors featuring the fractional quantum Hall effect [3], or quantum ferromagnets [29].

The rest of our paper is organized as follows: In Sec. II we introduce the microscopic Hamiltonian in a homogeneous magnetic field and an incident optical field as well as the Landau-quantized 2DEG wave functions. From the optically induced current density, we determine the scattered electric far field, allowing us to derive a time- and spectrally resolved intensity. In Sec. III, the elastic component of the resulting steady-state scattering spectrum is linked to the square of the Landau-quantized electron density distribution. This relation enables the reconstruction of the orbit structure of individual LLs (see Fig. 1) from angle-resolved XUV elastic scattering. The resulting energy-resolved electron densities are proportional to the probability density of LL wave functions $|\varphi_{\ell,m=0}(\mathbf{r}_\parallel)|^2$, featuring a characteristic maximum at the Larmor radius r_c.

II. THEORY

A. Landau states

We start by introducing the notation and single-particle wave functions we use in Secs. II B and II C for the calculation of the light-scattering signal from Landau levels. The effective mass Hamiltonian for a nonrelativistic electron moving in the $x - y$ plane in a perpendicular, homogeneous magnetic field B, reads [30]

$$H_0 = \hbar\omega_c\left(a^\dagger a + \tfrac{1}{2}\right), \tag{5}$$

with the cyclotron frequency $\omega_c = \frac{eB}{m^*}$, effective mass m^*, and bosonic ladder operators $a, a^\dagger$. The corresponding time-independent Schrödinger equation is

$$H_0|\varphi_{\ell,m}\rangle = E_\ell|\varphi_{\ell,m}\rangle. \tag{6}$$

Due to translational symmetry, each energy level

$$E_\ell = \hbar\omega_c\left(\ell + \tfrac{1}{2}\right) \tag{7}$$

is highly degenerate [6]. Since the energy of the LL $|\varphi_{\ell,m}\rangle$ is determined by ℓ, we refer to ℓ as the energy quantum number and to m as the degeneracy quantum number. The single-particle eigenstates are determined by

$$|\varphi_{\ell,m}\rangle = \frac{(b^\dagger)^m}{\sqrt{m!}}\frac{(a^\dagger)^\ell}{\sqrt{\ell!}}|\varphi_{0,0}\rangle, \tag{8}$$

with degeneracy ladder operators $b, b^\dagger$. The integer quantum numbers $\ell, m \geqslant 0$ are eigenvalues of $a^\dagger a$ and $b^\dagger b$, respectively. From Eq. (8), one obtains the LL wave function in position space:

$$\varphi_{\ell,m}(z_\mathbb{C}, z_\mathbb{C}^*) = \frac{i^\ell e^{-\frac{|z_\mathbb{C}|^2}{4l_B^2}}}{\sqrt{2\pi}l_B\sqrt{\ell!m!}}H_{\ell,m}\left(\frac{z_\mathbb{C}}{\sqrt{2}l_B}, \frac{z_\mathbb{C}^*}{\sqrt{2}l_B}\right), \tag{9}$$

with the complex in-plane coordinate $z_\mathbb{C} = x + iy$ and the complex Hermite polynomial $H_{\ell,m}$ [31].

In second quantization, the Hamiltonian for the electron gas in a static (classical) magnetic field $\mathbf{B} = \nabla \times \mathbf{A}_B$ and an incident optical field $\mathbf{A}_0$ is

$$H = \frac{1}{2m^*}\sum_{j_1 j_2}\langle\psi_{j_1}|\{\mathbf{p} + e(\mathbf{A}_B + \mathbf{A}_0)\}^2 + V_{\text{con}}(z)|\psi_{j_2}\rangle a_{j_1}^\dagger a_{j_2}, \tag{10}$$

and see also Fig. 2 for a schematic of the geometry. For notational reasons, we introduce $j_i = \{\ell_i, m_i\}$ as a compound quantum number consisting of ℓ_i and m_i. Here, $a_{j_i}^{(\dagger)}$ denotes the annihilation (creation) operator, $\mathbf{p}$ the momentum, and $V_{\text{con}}(z)$ an electron confinement potential restricting the motion to the x–y plane. We represent the static magnetic field B by the vector potential in symmetric gauge $\mathbf{A}_B(\mathbf{r}) = \frac{1}{2}\mathbf{B}\times\mathbf{r}$ and the additional optical field inducing the light scattering by $\mathbf{A}_0(\mathbf{r}, t)$, with $\mathbf{r}$ denoting the spatial vector $(\mathbf{r}_\parallel, z)$. The resulting eigenvalue problem,

$$H|\psi_j\rangle = \hbar\omega_j|\psi_j\rangle, \tag{11}$$

is solved by the separation ansatz,

$$\psi_j(\mathbf{r}) = \xi(z)\varphi_j(\mathbf{r}_\parallel), \tag{12}$$

with the out-of-plane confinement function $\xi(z)$ and LL wave function $\varphi_j(\mathbf{r}_\parallel)$ depending on the in-plane coordinates $\mathbf{r}_\parallel$.

B. Scattered electric field

The scattering contribution due to the optical current density is determined via the quadratic contribution in $\mathbf{A}_0$ in Eq. (10) [32]. The resulting operator for the optical current density is

$$\hat{\mathbf{j}}_0(\mathbf{r}, t) = -\frac{e^2}{m^*}\sum_{j_1 j_2}\psi_{j_1}^*(\mathbf{r})\mathbf{A}_0(\mathbf{r}, t)\psi_{j_2}(\mathbf{r})a_{j_1}^\dagger a_{j_2}. \tag{13}$$

As an approximation for a typical Gaussian beam with a spot size larger than the sample ($A = 10\,\mu\text{m}^2$ in this work), we assume a plane-wave incident optical field in a semiclassical approach (i.e., we assume classical excitation fields):

$$\begin{aligned}\mathbf{A}_0(\mathbf{r}, t) &= \mathbf{A}_0(e^{i(\mathbf{k}_0\cdot\mathbf{r}-\omega_0 t)} + \text{c.c.})\\ &= \mathbf{A}_0^{(+)}(\mathbf{r}, t) + \mathbf{A}_0^{(-)}(\mathbf{r}, t),\end{aligned} \tag{14}$$

with frequency ω_0, wave vector $\mathbf{k}_0 = \frac{\omega_0}{c}\mathbf{e}_z$, and $\mathbf{A}_0^{(+)}(\mathbf{r}, t) = (\mathbf{A}_0^{(-)}(\mathbf{r}, t))^\dagger$ (see Fig. 2). Consequently, the generated current density [Eq. (13)] emits an electric field, which in the frequency domain (scattered emission of frequency ω), at the detector position $\mathbf{r}$, reads [33]

$$\hat{\mathbf{E}}^{(+)}(\mathbf{r}, \omega) = \frac{i\omega\mu_0}{4\pi}\frac{e^{ikr}}{r}\int \mathrm{d}^3r'\,\hat{\mathbf{j}}_\perp^{(+)}(\mathbf{r}', \omega)e^{-i\mathbf{k}\cdot\mathbf{r}'}, \tag{15}$$

with the scattered wave vector $\mathbf{k} = \mathbf{e}_\mathbf{r}\frac{\omega}{c}$, $\mathbf{e}_\mathbf{r} = \frac{\mathbf{r}}{|\mathbf{r}|}$ being the unit vector in the direction of the detector, and the transverse current density operator $\hat{\mathbf{j}}_\perp^{(+)}(\mathbf{r}, \omega)$ as the source. We neglect corrections to the optical current density operator such that $\hat{\mathbf{j}}_\perp(\mathbf{r}, \omega) \approx \hat{\mathbf{j}}_0^\perp(\mathbf{r}, \omega)$ [cf. Eq. (13)], since the high-frequency incident optical field satisfies $\omega_0 \gg \omega_{j_1} - \omega_{j_2}$ compared to typical transition frequencies between LLs in the meV range [34]. Combining Eqs. (13), (14), and (15) and applying the (spatial) slowly varying envelope approximation, we obtain an expression for the time-dependent electric field operator at the detector:

$$\begin{aligned}\hat{\mathbf{E}}^{(+)}(\mathbf{r}, t) = -\frac{i\omega_0\mu_0 e^2}{4\pi m^* r}e^{i\omega_0 r/c}\sum_{j_1 j_2}\int \mathrm{d}^3r'\,\psi_{j_1}^*(\mathbf{r}')\mathbf{A}_0^\perp\psi_{j_2}(\mathbf{r}')\\ \times a_{j_1}^\dagger a_{j_2}e^{-i(\mathbf{k}-\mathbf{k}_0)\cdot\mathbf{r}'-i\omega_0 t}.\end{aligned} \tag{16}$$

For a detailed derivation see Appendix B.

C. Spectrum of the scattered light

To study an experimental observable of interest, we discuss the time- and spectrally resolved intensity $I(t, \mathbf{r}; \omega_\Gamma)$ at the detector position $\mathbf{r}$, assuming a point detector with bandpass filter centered at the detection frequency ω_Γ [35]:

$$\begin{aligned}I(t, \mathbf{r}; \omega_\Gamma) = \int_{-\infty}^{\infty}\mathrm{d}t_1\int_{-\infty}^{\infty}\mathrm{d}t_2\,T_\Gamma^*(\omega_\Gamma, t - t_1)T_\Gamma(\omega_\Gamma, t - t_2)\\ \times G(\mathbf{r}; t_1, t_2).\end{aligned} \tag{17}$$

Here, $G(\mathbf{r}; t_1, t_2)$ defines the field correlation function

$$G(\mathbf{r}; t_1, t_2) = \langle\mathcal{T}\{\hat{\mathbf{E}}^{(-)}(\mathbf{r}, t_1)\hat{\mathbf{E}}^{(+)}(\mathbf{r}, t_2)\}\rangle, \tag{18}$$

where $\mathcal{T}$ denotes time ordering, and

$$T_\Gamma(\omega_\Gamma, t) = \Gamma\Theta(t)e^{-(i\omega_\Gamma+\Gamma)t} \tag{19}$$

represents the spectral bandpass filter with the spectral width $\Gamma \ll \omega_\Gamma$ (see Fig. 2). We emphasize that the detection frequency ω_Γ is not the Fourier transform of the detection time window t.

In the steady-state limit ($t \to \infty$), the stationary scattered spectrum is given by [35]

$$\begin{aligned}S(\mathbf{r}; \omega_\Gamma) &= \frac{1}{\Gamma}\lim_{t\to\infty} I(t, \mathbf{r}; \omega_\Gamma)\\ &= \int_0^\infty \mathrm{d}\tau\, e^{-i\omega_\Gamma\tau}e^{-\Gamma\tau}G(\mathbf{r}; \tau) + \text{c.c.},\end{aligned} \tag{20}$$

with the steady-state field correlation function [35,36]:

$$G(\mathbf{r};\tau) = \lim_{t\to\infty} G(\mathbf{r};t+\tau,t). \tag{21}$$

Next, inserting the electric field at the detector, Eq. (16), into Eq. (18), we obtain the field correlation function:

$$G(\mathbf{r};t+\tau,t) = \sum_{\substack{j_1 j_2\\ j_3 j_4}} \langle a^\dagger_{j_1}(t+\tau)a_{j_2}(t+\tau)a^\dagger_{j_3}(t)a_{j_4}(t)\rangle \times \mathcal{S}_{j_1 j_2 j_3 j_4}(\mathbf{k}-\mathbf{k}_0)\left(\frac{\omega_0 r_0}{r}\right)^2 |\mathbf{A}_0^\perp|^2 e^{i\omega_0\tau}, \tag{22}$$

with the magnitude of the detector position $r = |\mathbf{r}|$ and the Thomson scattering length $r_0 = \frac{\mu_0 e^2}{4\pi m^*}$. We have also identified the scattering matrix,

$$\mathcal{S}_{j_1 j_2 j_3 j_4}(\mathbf{q}) = \int \mathrm{d}^3 r'\, \psi^*_{j_1}(\mathbf{r}')\psi_{j_2}(\mathbf{r}')e^{i\mathbf{q}\cdot\mathbf{r}'} \times \int \mathrm{d}^3 r''\, \psi^*_{j_3}(\mathbf{r}'')\psi_{j_4}(\mathbf{r}'')e^{-i\mathbf{q}\cdot\mathbf{r}''}, \tag{23}$$

with the scattering vector $\mathbf{q} = \mathbf{k} - \mathbf{k}_0$.

The LL operator dynamics is dominated by their intrinsic time dependency,

$$a_j(t) = a_j e^{-i\omega_j t}, \tag{24}$$

with ω_j defined in Eq. (11). The free-energy solution [Eq. (24)] neglects the dynamics of the electronic operators $a_j^{(\dagger)}$ induced by $\mathbf{A}_0$, which, if taken into account, would result in higher-order contributions of at least $\mathcal{O}(\mathbf{A}_0^4)$ in a series expansion of the electric field correlation [Eq. (22)]. Similarly, we can restrict ourselves to occupations $f_j = \langle a_j^\dagger a_j\rangle$ and neglect transitions between LLs, $\langle a^\dagger_{j_1} a_{j_2}\rangle$ with $j_1 \neq j_2$.

In the Hartree-Fock approximation for the electron operators (see Appendix C 1), the steady-state field correlation function [Eq. (21)] reads

$$G(\mathbf{r};\tau) = \left(\frac{\omega_0 r_0}{r}\right)^2 \left|\mathbf{A}_0^\perp\right|^2 e^{i\omega_0\tau} \sum_{j_1 j_2} (f_{j_1} f_{j_2} \mathcal{S}_{j_1 j_1 j_2 j_2}(\mathbf{q}) + e^{i(\omega_{j_1}-\omega_{j_2})\tau} f_{j_1}(1-f_{j_2})\mathcal{S}_{j_1 j_2 j_2 j_1}(\mathbf{q})). \tag{25}$$

In the effective mass approximation, $\varphi_j(\mathbf{r}_\parallel)$ and $\xi(z)$ are spatially constant over a unit cell of the crystal lattice, so the scattering matrix [Eq. (23)] simplifies to

$$\mathcal{S}_{j_1 j_2 j_3 j_4}(\mathbf{q}_\parallel) = \int \mathrm{d}^2 r_\parallel\, \varphi^*_{j_1}(\mathbf{r}_\parallel)e^{i\mathbf{q}_\parallel\cdot\mathbf{r}_\parallel}\varphi_{j_2}(\mathbf{r}_\parallel) \times \int \mathrm{d}^2 r'_\parallel\, \varphi^*_{j_3}(\mathbf{r}'_\parallel)e^{-i\mathbf{q}_\parallel\cdot\mathbf{r}'_\parallel}\varphi_{j_4}(\mathbf{r}'_\parallel), \tag{26}$$

with the in-plane component of the scattering vector $\mathbf{q}_\parallel$. Due to a thin-film approximation, Eq. (26) becomes independent of the z component of the scattering vector $\mathbf{q}$; see Appendix C 2 for details.

We next combine Eqs. (20), (24), (25), and (26) and obtain, in the limit of an ideal filter $\Gamma \to 0$, the steady-state scattering spectrum:

$$S(r;\omega_\Gamma,\mathbf{q}_\parallel) = 2\pi\left(\frac{\omega_0 r_0}{r}\right)^2 |\mathbf{A}_0^\perp|^2 \sum_{j_1 j_2} (\delta(\omega_\Gamma-\omega_0) f_{j_1} f_{j_2} \times \mathcal{S}_{j_1 j_1 j_2 j_2}(\mathbf{q}_\parallel) + \delta(\omega_\Gamma-\omega_0+\omega_{j_2}-\omega_{j_1}) \times f_{j_1}(1-f_{j_2})\mathcal{S}_{j_1 j_2 j_2 j_1}(\mathbf{q}_\parallel)), \tag{27}$$

with the compound quantum number $j_i = \{\ell_i, m_i\}$. For a detailed derivation, see Appendix C 3. Due to energy conservation of the in- and out-scattered wave, the first term can be attributed to *elastic scattering* of light $\mathbf{A}_0$ at occupied LLs. In contrast, the second term describes inelastic scattering with an energy gain or loss corresponding to an electronic transition between an occupied state j_1 and an unoccupied state j_2.

Due to finite sample size, the degeneracy quantum number m is limited to [30]

$$m \leqslant m_{\mathrm{lim}} = \mathrm{floor}\left[\frac{A}{2\pi l_B^2}\right], \tag{28}$$

using the floor function, and for simplicity, we assume a circular sample with area $A = \pi R^2 \gg \pi l_B^2$; see Fig. 1. In this limit, the occupations can be expressed as

$$f_{\ell,m}(B) = f_\ell(B)\,\Theta(m_{\mathrm{lim}} - m). \tag{29}$$

We emphasize that the Heaviside step function is only introduced for technical reasons as no LLs with $m > m_{\mathrm{lim}}$ exist. For the energy quantum number ℓ, then $f_\ell(B)$ is given by a Fermi-Dirac distribution,

$$f_\ell(B) = \left(e^{\frac{E_\ell - \mu(T,B)}{k_B T}} + 1\right)^{-1}, \tag{30}$$

with E_ℓ given in Eq. (7). The chemical potential of a 2DEG for low temperatures ($k_B T \ll \hbar\omega_\mathrm{c}$) reads [37]

$$\mu(T,B) = -k_B T \ln\left(\frac{w\cosh a + \sqrt{1+w^2\sinh^2 a}}{1-w}\right) + \hbar\omega_\mathrm{c}(\ell_F+1), \tag{31}$$

with the abbreviations $w = \ell_F - \nu + 1$ and $a = \frac{\hbar\omega_\mathrm{c}}{2k_B T}$. Here, $\ell_F = \mathrm{floor}[\nu]$ is the highest occupied LL and follows from the filling factor ν [30],

$$\nu = \bar{n}_\mathrm{el} 2\pi l_B^2, \tag{32}$$

which depends on the spatially homogeneous electron density $\bar{n}_\mathrm{el}$ without a magnetic field due to doping and the magnetic length l_B, which determines the area occupied by a single Landau quantized electron; cf. Fig. 1. For clarity, the density of states DOS(E) of the LLs is schematically depicted in Fig. 3 together with the Fermi-Dirac distribution $f_\ell(E,T,B)$ [Eq. (30)], for a temperature of $T = 2$ K ($T = 10$ K). The occupied LLs are hatched (shaded) in dark (light) purple with the highest occupied LL, $\ell_F = 7$ ($\ell_F = 8$).

For this paper, we choose the representative parameters listed in Table I. We note that the magnetic field B (and thereby $\hbar\omega_\mathrm{c}$ and l_B), the temperature T, and the incident frequency ω_0 can be adjusted to optimize the experimental resolution.

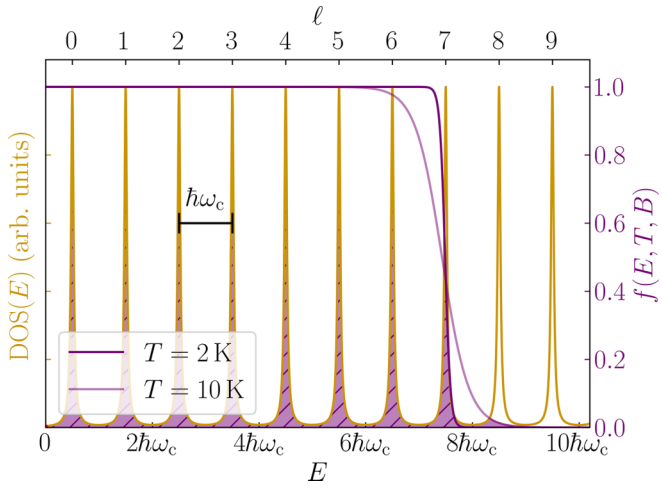


FIG. 3. Schematic of the density of states DOS(E) (orange) of the LLs with energy quantum number ℓ and Fermi-Dirac distribution $f_\ell(E,T,B)$ [Eq. (30)], in dark (light) purple for the temperature $T = 2\,\mathrm{K}$ ($T = 10\,\mathrm{K}$). Occupied LLs are hatched (shaded) in dark (light) purple with the highest occupied LL $\ell_F = 7$ ($\ell_F = 8$). The parameters are provided in Table I. For clarity, an artificial linewidth $\hbar\gamma = 0.2$ meV has been applied, where $\hbar\omega_c \approx 3.5$ meV.

We briefly highlight the dependency of the occupations [Eq. (29)] on the magnetic field. The degeneracy of the LLs m_{lim} [Eq. (28)] increases with increasing B, such that the filling factor ν [Eq. (32)] decreases. Therefore, the highest occupied LL ℓ_F decreases with B, which is reflected in the occupations $f_{\ell,m}(B)$.

D. Elastic scattering

One goal of this work is to determine the in-plane spatial extension of Landau orbits from light-scattering data. We focus on the case $\omega_\Gamma = \omega_0$, where the frequencies of scattered and incident light coincide, i.e., the elastic scattering excluding processes with energy transfer between the incident electric field and the electronic system. In this limit, the second term of Eq. (27) accounting for inelastic scattering only contributes if $\omega_{j_1} = \omega_{j_2}$, requiring $\ell_1 = \ell_2$. At sufficiently low temperatures, the Fermi-Dirac distribution [Eq. (30)] ensures that the product $f_{\ell_1,m_1}(1 - f_{\ell_1,m_2}) \approx 0$, such that these transitions within the same LL undergo Pauli blocking. We may therefore neglect all inelastic contributions, and the steady-state spectrum [Eq. (27)] simplifies to an expression fully determined by elastic scattering:

$$S(r;\omega_\Gamma,\mathbf{q}_\parallel,B) = 2\pi\left(\frac{\omega_0 r_0}{r}\right)^2 |\mathbf{A}_0^\perp|^2 \delta(\omega_\Gamma - \omega_0) \times \sum_{j_1 j_2} f_{j_1}(B) f_{j_2}(B) \mathcal{S}_{j_1 j_1 j_2 j_2}(\mathbf{q}_\parallel, B). \quad (33)$$

The spatial extension of the LLs (see Fig. 1) is encoded in the momentum dependence $\mathbf{q}_\parallel$ of Eq. (33).

To focus on this aspect, we integrate the spectrum over ω_Γ:

$$S(r;\mathbf{q}_\parallel,B) = 2\pi\left(\frac{\omega_0 r_0}{r}\right)^2 |\mathbf{A}_0^\perp|^2 \times \sum_{j_1 j_2} f_{j_1}(B) f_{j_2}(B) \mathcal{S}_{j_1 j_1 j_2 j_2}(\mathbf{q}_\parallel, B). \quad (34)$$

In Appendix D, we rewrite the in-plane position $\mathbf{r}_\parallel$ of the scattering matrix [Eq. (26)] in terms of LL ladder operators in the Taylor expansion of the exponential. This allows us to determine the elastic-scattering matrix element $\mathcal{S}_{j_1 j_1 j_2 j_2}(\mathbf{q}_\parallel)$ needed to evaluate Eq. (34):

$$S(r;q_\parallel,B) = 2\pi\left(\frac{\omega_0 r_0}{r}\right)^2 |\mathbf{A}_0^\perp|^2 e^{-l_B^2 q_\parallel^2} \left(L^{(1)}_{m_{\mathrm{lim}}}\left(\frac{l_B^2 q_\parallel^2}{2}\right)\right)^2 \times \left(\sum_{\ell=0}^{\infty} f_\ell(B) L_\ell\left(\frac{l_B^2 q_\parallel^2}{2}\right)\right)^2, \quad (35)$$

with the magnitude $q_\parallel = |\mathbf{q}_\parallel| = |\mathbf{k}_\parallel - \mathbf{k}_{0\parallel}|$ [cf. Eq. (4)], the Laguerre polynomial L_ℓ and the associated Laguerre polynomial $L^{(1)}_{m_{\mathrm{lim}}}$ [38]. The analysis and application of Eq. (35) (cf. Sec. III) constitutes one of the main results of this work.

TABLE I. Parameters.

Parameter	Value	Unit	Reference
m_e	5.68568	$\mathrm{fs^2\,eV\,nm^{-2}}$	
$\hbar$	0.658212	eV fs	
k_B	0.0861745	$\mathrm{meV\,K^{-1}}$	
m^* (GaAs)	$0.067\,m_e$	$\mathrm{fs^2\,eV\,nm^{-2}}$	[49]
$\bar{n}_{\mathrm{el}}$	0.0036	$\mathrm{nm^{-2}}$	[45]
A	10	$\mu\mathrm{m}^2$	
B	2	T	
T	2	K	

III. DISCUSSION

A. Elastic-scattering spectrum

The elastic-scattering spectrum $S(r;q_\parallel,B)$ [Eq. (35)] depends on the magnitude of the scattering vector $q_\parallel = |\mathbf{k}_\parallel - \mathbf{k}_{0\parallel}|$. It incorporates the scattering angle θ between the incident optical field and the detected light; see Fig. 2. For the hypothetical $q_\parallel = 0$, corresponding to parallel incidence and detection (not observable in dark-field scattering), the elastic-scattering spectrum can be evaluated in a compact form,

$$S(r;q_\parallel = 0) = 2\pi\left(\frac{\omega_0 r_0}{r}\right)^2 |\mathbf{A}_0^\perp|^2 N^2, \quad (36)$$

with the total number of electrons N in the 2DEG.

This result is independent of the magnetic field, but scales quadratically with the sample area A and spatially averaged electron density $\bar{n}_{\mathrm{el}}$,

$$S(r;q_\parallel = 0) \propto N^2 = \bar{n}_{\mathrm{el}}^2 A^2. \quad (37)$$

Each of the N electrons emits a partial wave with equal electric field amplitude, whose superposition at the detector is proportional to the electron number N [39].

For a large degeneracy of the LLs, $m_{\mathrm{lim}} \gg 1$, which is satisfied for $A \gg \pi l_B^2$ (cf. Fig. 1), we identify the diffracted intensity distribution of a circular disk [39,40] of radius $R \approx \sqrt{2 m_{\mathrm{lim}} l_B^2}$ in the first line of the elastic-scattering spectrum,

Eq. (35):

$$\left(L^{(1)}_{m_{\rm lim}}\left(\frac{l_B^2 q_\parallel^2}{2}\right)\right)^2 = \left(\frac{\bar{n}_{\rm el}A}{\nu}\frac{2J_1(q_\parallel R)}{q_\parallel R}\right)^2, \tag{38}$$

with the Bessel function of the first kind, $J_{\alpha=1}$, and the filling factor ν. Thus, the elastic-scattering spectrum [Eq. (35)] is a product of a term accounting for the Landau orbits and a term accounting for the light scattering at a circular disk, determined only by the sample geometry (which is independent of the magnetic field), Eq. (38):

$$S(r;q_\parallel,B) = \underbrace{\left(\frac{e^{-\frac{l_B^2 q_\parallel^2}{2}}}{\nu}\sum_{\ell=0}^{\infty} f_\ell(B) L_\ell\left(\frac{l_B^2 q_\parallel^2}{2}\right)\right)^2}_{\text{LL scattering } S_{\rm LL}(q_\parallel,B)} \times \underbrace{\left(\frac{2J_1(q_\parallel R)}{q_\parallel R}\right)^2 S(r;q_\parallel=0)}_{\text{disk scattering } S_{\rm D}(r;q_\parallel)}. \tag{39}$$

To support our interpretation [Eqs. (38) and (39)], we derive the elastic-scattering spectrum without a magnetic field in Appendix E, i.e., scattering at a free 2DEG (Drude model) in a disk-shaped sample:

$$S_{\rm D}(r;q_\parallel) = S(r;q_\parallel=0)\left(\frac{2J_1(q_\parallel R)}{q_\parallel R}\right)^2, \tag{40}$$

where we identified the full elastic-scattering spectrum for parallel incidence and detection, Eq. (36).

In the following we connect the momentum dependence $\mathbf{q}_\parallel$ of the scattering spectrum to the spatial structure of Landau orbits; see Fig. 1. Combining Eqs. (26) and (34) allows us to identify the electron density distribution in momentum space,

$$\begin{aligned} n_{\rm el}(\mathbf{q}_\parallel) &= \int {\rm d}^2 r_\parallel\, e^{-i\mathbf{q}_\parallel\cdot\mathbf{r}_\parallel} n_{\rm el}(\mathbf{r}_\parallel) \\ &= \int {\rm d}^2 r_\parallel\, e^{-i\mathbf{q}_\parallel\cdot\mathbf{r}_\parallel} \sum_j f_j(B)\varphi_j^*(\mathbf{r}_\parallel)\varphi_j(\mathbf{r}_\parallel), \end{aligned} \tag{41}$$

in the elastic-scattering spectrum, Eq. (35):

$$S(r;\mathbf{q}_\parallel,B) = 2\pi\left(\frac{\omega_0 r_0}{r}\right)^2 |\mathbf{A}_0^\perp|^2 |n_{\rm el}(\mathbf{q}_\parallel)|^2. \tag{42}$$

Note that we have to distinguish between the spatially homogeneous electron density $\bar{n}_{\rm el} = N/A$ without a magnetic field and the momentum-resolved electron density distribution $n_{\rm el}(\mathbf{q}_\parallel)$ [Eq. (41)]. Comparing Eqs. (36), (39), and (42) yields the electron density distribution in momentum space for a large sample size $A \gg \pi l_B^2$, i.e., $m_{\rm lim} \gg 1$ (see Fig. 1),

$$n_{\rm el}(q_\parallel) = \frac{1}{\nu} e^{-\frac{l_B^2 q_\parallel^2}{2}} \sum_{\ell=0}^{\infty} f_\ell(B) L_\ell\left(\frac{l_B^2 q_\parallel^2}{2}\right) \times \bar{n}_{\rm el} A\left(\frac{2J_1(q_\parallel R)}{q_\parallel R}\right), \tag{43}$$

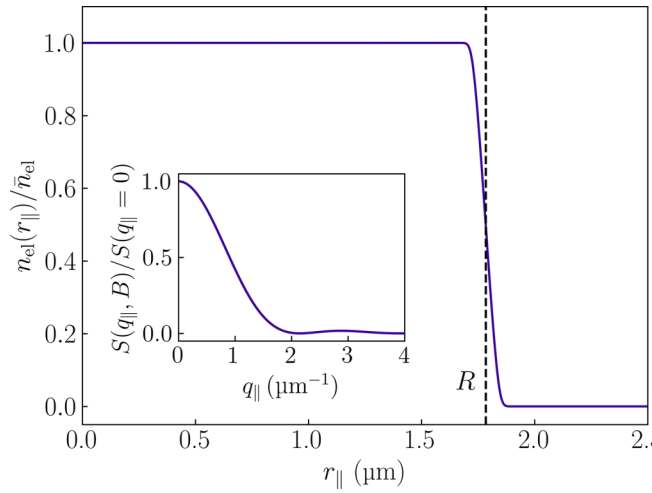


FIG. 4. Normalized electron density distribution [Eq. (44)] as a function of the radius $r_\parallel$ for the parameters provided in Table I. The sample radius R is indicated with a dashed black line. The inset shows the full normalized elastic-scattering spectrum [cf. Eqs. (35) and (36)], which is dominated by the B-independent scattering by the sample geometry (circular disk); cf. Eq. (40).

or, in position space,

$$\frac{n_{\rm el}(r_\parallel)}{\bar{n}_{\rm el}} = \frac{R}{\nu}\int_0^\infty {\rm d}q_\parallel \left(e^{-\frac{l_B^2 q_\parallel^2}{2}} J_0(q_\parallel r_\parallel) J_1(q_\parallel R) \times \sum_{\ell=0}^{\infty} f_\ell(B) L_\ell\left(\frac{l_B^2 q_\parallel^2}{2}\right)\right). \tag{44}$$

Equation (44) can easily be numerically integrated, and the result is shown in Fig. 4. All relevant parameters are provided in Table I. In accordance with the chosen parameters, the electron density distribution remains constant before it rapidly drops to zero at the sample radius R, indicated with a dashed black line.

We now address the question of how one can determine real-space information on the Landau orbits (see Fig. 1) from this data; cf. Eqs. (42) and (44), which can be measured in light-scattering experiments. The electron density distribution $n_{\rm el}(q_\parallel)$, defined in Eq. (43), is a product of the sample geometry contribution $2\bar{n}_{\rm el}AJ_1(q_\parallel R)/(q_\parallel R)$ (2D Fourier transform of a disk; cf. Appendix E) and a contribution accounting for the Landau orbits, specifically

$$\frac{1}{\nu} e^{-\frac{l_B^2 q_\parallel^2}{2}} \sum_{\ell=0}^{\infty} f_\ell(B) L_\ell\left(\frac{l_B^2 q_\parallel^2}{2}\right). \tag{45}$$

Therefore, the normalized electron density distribution in position space ($\mathbf{r}_\parallel$) [Eq. (44)] constitutes a convolution of the disklike sample geometry and the spatial extension of the Landau orbits. Furthermore, in Eq. (45) the exponential $\exp(-l_B^2 q_\parallel^2/2)$ acts like a low-pass filter, smoothing over spatial variations in the electron density distribution below the magnetic length, i.e., below the electron localization length scale; cf. Eq. (44). This observation allows us to address the LL extension; cf. Sec. III B.

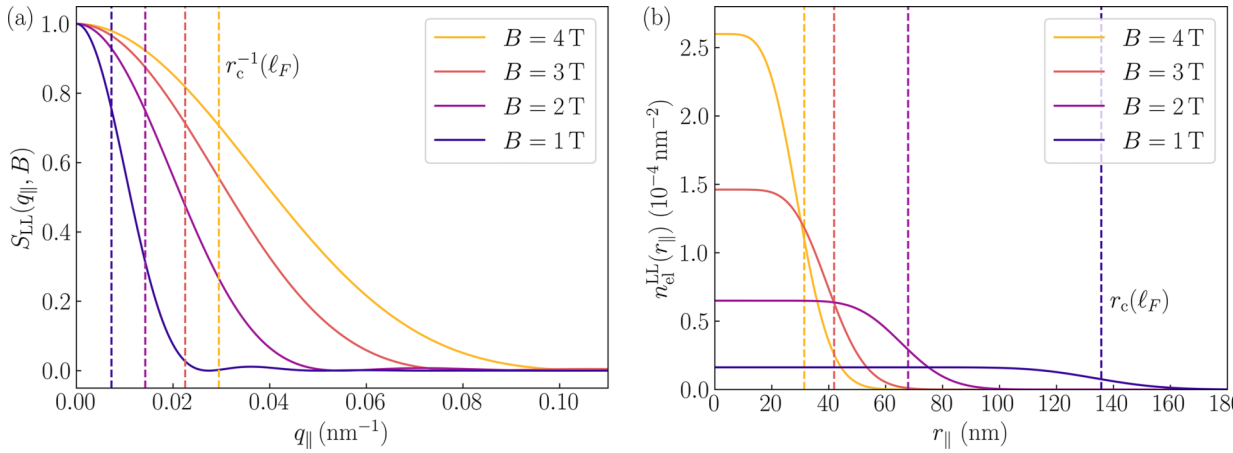


FIG. 5. (a) LL scattering spectrum $S_{\mathrm{LL}}(q_\parallel, B)$ [Eq. (46)] as a function of $q_\parallel$, and (b) LL electron density distribution $n_{\mathrm{el}}^{\mathrm{LL}}(r_\parallel)$ [Eq. (49)] as a function of the radius $r_\parallel$ for magnetic fields between $B = 1\,\mathrm{T}$ and $B = 4\,\mathrm{T}$ and the parameters provided in Table I. Dashed lines indicate in (a) the inverse Larmor radius $r_c^{-1}(\ell_F)$ and (b) the Larmor radius $r_c(\ell_F)$ [Eq. (1)] of the highest occupied LL ℓ_F.

B. Spatial extension of Landau orbits

By exploiting the convolution theorem, the product of the disk and Landau orbit terms in momentum space [see Eq. (44)] translates to a convolution in position space. Therefore, the spatial structure of Landau orbits (see Fig. 1) is masked by the disklike sample geometry in Fig. 4: the spatial delocalization of a Landau-quantized electron in the magnetic field is determined by the Larmor radius r_c. Since $R \gg r_c$ (cf. Fig. 1), the angular range of (B-independent) scattering at the disk geometry is significantly smaller than for scattering by Landau orbits, i.e., deviations from scattering at the disklike sample geometry [Eq. (39)], are small even for magnetic fields with a few tesla magnitude; see inset of Fig. 4. Therefore, we propose a different method to detect details on the length scale of r_c, as described below.

Dividing the full elastic-scattering spectrum [Eq. (39)] by the spectrum without a magnetic field [Eq. (40)] yields the normalized elastic scattering by the Landau orbits without the influence of the sample geometry,

$$S_{\mathrm{LL}}(q_\parallel, B) \equiv \frac{S(r; q_\parallel, B)}{S_{\mathrm{D}}(r; q_\parallel)} = \frac{e^{-l_B^2 q_\parallel^2}}{\nu^2}\left(\sum_{\ell=0}^{\infty} f_\ell(B) L_\ell\left(\frac{l_B^2 q_\parallel^2}{2}\right)\right)^2. \tag{46}$$

Experimentally, one could similarly obtain the LL scattering spectrum $S_{\mathrm{LL}}(q_\parallel, B)$ by normalizing the spectrum with an applied magnetic field, to the spectrum without a magnetic field. The LL scattering spectrum deviates from the corresponding differential spectrum only by a constant:

$$\frac{S(r; q_\parallel, B) - S_{\mathrm{D}}(r; q_\parallel)}{S_{\mathrm{D}}(r; q_\parallel)} = S_{\mathrm{LL}}(q_\parallel, B) - 1. \tag{47}$$

In the hypothetical limit of parallel incidence and detection, we obtain for the LL scattering spectrum $S_{\mathrm{LL}}(q_\parallel = 0, B) = 1$, though this limit is not observable in the proposed dark-field scattering [41], which excludes $q_\parallel = 0$.

A typical solution of Eq. (46) is displayed as a function of $q_\parallel$ for varying magnetic fields in Fig. 5(a). The parameters used are listed in Table I. We observe that the width of the spectrum in momentum space ($q_\parallel$) is determined by the inverse Larmor radius $r_c^{-1}(\ell_F)$ of the highest occupied LL ℓ_F, indicated by dashed lines in Fig. 5(a). Experimentally, this width can be related to the angular width of the scattering angle θ; see Fig. 2. The Larmor radius r_c decreases with increasing magnetic field, which increases the scattering angle and thus angular width, reflected in a larger in-plane scattering vector in Fig. 5(a).

Note that the relative change in the width of S_{LL} decreases for large B, since the inverse Larmor radius $r_c^{-1} \propto l_B^{-1} \propto \sqrt{B}$, which determines the width of S_{LL} in $q_\parallel$, increases less than linearly with respect to B.

To illustrate the magnetic field sensitivity of the LL scattering spectrum S_{LL}, its magnetic field derivative $\partial_B S_{\mathrm{LL}}(q_\parallel, B)$ is depicted in Fig. 6 (lower panel). It becomes evident that moderate fields $B \lesssim 5\,\mathrm{T}$ are favorable for maximizing the magnetic-field-induced variation of the LL scattering spectrum. Interestingly, Fig. 6 (lower panel) reveals a steplike structure in $\partial_B S_{\mathrm{LL}}(q_\parallel, B)$ as a function of B. The steps occur

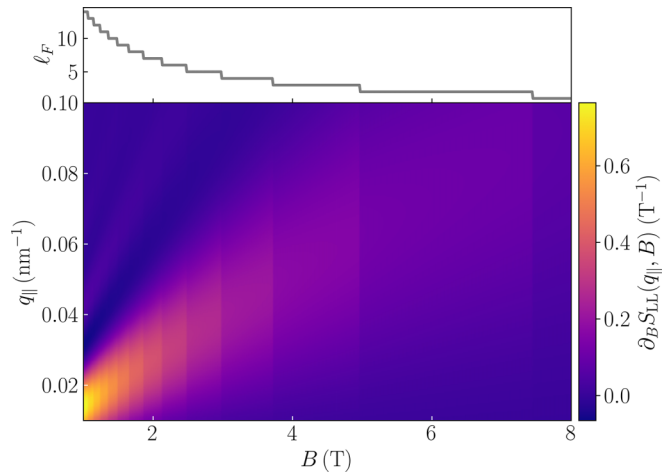


FIG. 6. Lower panel: Magnetic field derivative of the LL scattering spectrum $\partial_B S_{\mathrm{LL}}(q_\parallel, B)$ as a function of the magnetic field B and in-plane scattering vector $q_\parallel$. Upper panel: Highest occupied LL ℓ_F as a function of the magnetic field B. At magnetic fields where ℓ_F changes, steps appear in $\partial_B S_{\mathrm{LL}}$.

when an additional LL begins to populate, i.e., when the highest occupied LL ℓ_F changes (cf. upper panel in Fig. 6).

To support our interpretation of the LL scattering spectrum S_{LL}, we divide $n_{\mathrm{el}}(q_\parallel)$ [Eq. (43)] by $2\bar{n}_{\mathrm{el}}AJ_1(q_\parallel R)/(q_\parallel R)$, thereby defining the LL electron density distribution $n_{\mathrm{el}}^{\mathrm{LL}}(q_\parallel)$ similar to Eq. (46), to recover the spatial information of the Landau orbits:

$$n_{\mathrm{el}}^{\mathrm{LL}}(q_\parallel) = \frac{1}{\nu} e^{-\frac{l_B^2 q_\parallel^2}{2}} \sum_{\ell=0}^{\infty} f_\ell(B) L_\ell\left(\frac{l_B^2 q_\parallel^2}{2}\right). \tag{48}$$

A 2D Fourier transform into position space yields

$$\begin{aligned} n_{\mathrm{el}}^{\mathrm{LL}}(r_\parallel) &= \frac{\bar{n}_{\mathrm{el}}}{\nu^2} \sum_{\ell=0}^{\infty} \frac{f_\ell(B)}{\ell!} \left(\frac{r_\parallel^2}{2l_B^2}\right)^\ell e^{-\frac{r_\parallel^2}{2l_B^2}} \\ &= \frac{1}{\nu} \sum_{\ell=0}^{\infty} f_\ell(B) |\varphi_{\ell,m=0}(\mathbf{r}_\parallel)|^2, \end{aligned} \tag{49}$$

where we identified the probability density of the LL wave function $\varphi_{\ell,m=0}(\mathbf{r}_\parallel)$; cf. Eq. (9). For a detailed derivation see Appendix F. As shown in Fig. 1, the degeneracy quantum number m determines the guiding center $r_{\mathrm{g}}(m)$ of the Larmor orbits. The superposition $\sum_{m=0}^{m_{\mathrm{lim}}} |\varphi_{\ell,m}(\mathbf{r}_\parallel)|^2$ of LL wave functions with a given ℓ but different guiding centers $r_{\mathrm{g}}(m)$ thus resembles the disklike sample geometry. This influence of the sample geometry is eliminated in the LL scattering spectrum $S_{\mathrm{LL}}(q_\parallel, B)$, since dividing by the disk scattering $S_{\mathrm{D}}(r; q_\parallel)$ corresponds to shifting all guiding centers $r_{\mathrm{g}}(m)$ to their minimal value $r_{\mathrm{g}}(m=0) = l_B$.

The angle-integrated probability density distribution of the LL wave functions with $m = 0$ is maximal at the Larmor radius:

$$\left[\frac{\partial}{\partial r_\parallel} 2\pi r_\parallel |\varphi_{\ell,m=0}(\mathbf{r}_\parallel)|^2\right]\Big|_{r_{\mathrm{c}}} = 0. \tag{50}$$

The LL electron density distribution is proportional to the sum over all occupied $|\varphi_{\ell,m=0}(\mathbf{r}_\parallel)|^2$ [cf. Eq. (49)]; hence, its width is determined by the Larmor radius $r_{\mathrm{c}}(\ell_F)$ of the highest occupied LL. Accordingly, the width of the LL scattering spectrum $S_{\mathrm{LL}}(q_\parallel, B)$ (momentum space) is given by the inverse Larmor radius $r_{\mathrm{c}}^{-1}(\ell_F)$.

The LL electron density distribution $n_{\mathrm{el}}^{\mathrm{LL}}(r_\parallel)$ is evaluated for varying magnetic fields in Fig. 5(b). The width of $n_{\mathrm{el}}^{\mathrm{LL}}(r_\parallel)$ and the Larmor radius $r_{\mathrm{c}}(\ell_F)$ of the highest occupied LL, indicated by dashed lines in Fig. 5(b), decrease similarly for an increasing magnetic field.

Furthermore, we are able to distinguish the contribution of electrons in energetically different LLs in Eq. (49) by evaluating the terms of the sum over ℓ individually:

$$n_{\mathrm{el}}^{\ell}(r_\parallel) = \frac{f_\ell(B)}{\nu} |\varphi_{\ell,m=0}(\mathbf{r}_\parallel)|^2, \tag{51}$$

such that

$$n_{\mathrm{el}}^{\mathrm{LL}}(r_\parallel) = \sum_{\ell} n_{\mathrm{el}}^{\ell}(r_\parallel). \tag{52}$$

Analogous to $n_{\mathrm{el}}^{\mathrm{LL}}(r_\parallel)$, the energy-resolved electron density distribution $n_{\mathrm{el}}^{\ell}(r_\parallel)$ [Eq. (51)] represents the spatial extension of all electrons in a given LL ℓ with their guiding centers r_{g} shifted to its minimal value $r_{\mathrm{g}}(m=0) = l_B$; cf. Fig. 1.

We highlight that the energy-resolved electron density distribution $n_{\mathrm{el}}^{\ell}(r_\parallel)$ is also accessible from a measured spectrum. Utilizing the orthogonality relation of the Laguerre polynomials [38],

$$\int_0^\infty \mathrm{d}x\, e^{-x} L_{\ell'}(x) L_\ell(x) = \delta_{\ell,\ell'}, \tag{53}$$

we multiply Eq. (48), i.e., the possible observable in a scattering experiment, by $\nu L_\ell(l_B^2 q_\parallel^2/2)$ and integrate over $(l_B^2 q_\parallel^2/2)$ to represent the occupations:

$$f_\ell(B) = \nu \int_0^\infty \mathrm{d}\left(\frac{l_B^2 q_\parallel^2}{2}\right) L_\ell\left(\frac{l_B^2 q_\parallel^2}{2}\right) n_{\mathrm{el}}^{\mathrm{LL}}(q_\parallel). \tag{54}$$

Inserting $f_\ell(B)$ [Eq. (54)] into Eq. (51) thus yields the energy-resolved electron density distribution $n_{\mathrm{el}}^{\ell}(r_\parallel)$.

The energy-resolved electron density distribution $n_{\mathrm{el}}^{\ell}(r_\parallel)$ is evaluated in Fig. 7(a) for the energy quantum numbers from $\ell = 0$ to $\ell = 7$. It exhibits a single peak whose position shifts to higher radii for increasing ℓ. We assign the peaks in the energy-resolved electron density distribution [Eq. (51)] to the respective Landau orbit ℓ. The summation over all Landau orbits results in the LL electron density distribution $n_{\mathrm{el}}^{\mathrm{LL}}(r_\parallel)$, as shown with a black line in Fig. 7(a).

In Fig. 7(b) we also evaluate the angle-integrated energy-resolved electron density distribution $(2\pi r_\parallel) n_{\mathrm{el}}^{\ell}(r_\parallel)$ [cf. Eq. (51)], which includes the polar area element in 2D space and therefore weights contributions from larger radii stronger. The angle-integrated energy-resolved electron density distribution is maximal at the Larmor radius—in agreement with Eqs. (50) and (51) and the interpretation of the peaks as Landau orbits. Furthermore, Fig. 7(b) and the inset of Fig. 1 are consistent if the factor $f_\ell(B)/\nu$ in Eq. (51) is taken into account. The amplitude of the peak assigned to $\ell_F = 7$ is smaller compared to the other peaks ($\ell < \ell_F$), since it is only partially occupied for the chosen parameters (cf. Table I), i.e., $f_{\ell_F=7} < 1$. Due to the finite number of electrons, higher LLs $\ell > \ell_F$ are unoccupied, such that $n_{\mathrm{el}}^{\mathrm{LL}}(r_\parallel)$ drops at $r_{\mathrm{c}}(\ell_F) = l_B\sqrt{2\ell_F + 1}$, as shown in Fig. 5(b).

IV. CONCLUSIONS

We have demonstrated how the probability density of Landau-quantized electrons in a 2DEG can be accessed optically through elastic scattering. Starting from a microscopic Hamiltonian for a 2DEG in a perpendicular static magnetic field under XUV illumination, we derived the angle-resolved far-field scattering spectrum from the optically induced current density. The elastic component of this scattering was shown to be directly related to the Fourier transform of the spatially resolved electron density distribution. For future research, it would be interesting to expand this theory by also incorporating the inelastic-scattering component [second contribution in Eq. (27)] to account for inter-LL transitions, thereby enhancing its applicability.

In order to isolate the spatial information of the Landau orbits therein, we introduced the LL scattering spectrum $S_{\mathrm{LL}}(q_\parallel, B)$ by normalizing the magnetic-field-dependent $(B \neq 0)$ scattering spectrum to the spectrum in absence of a

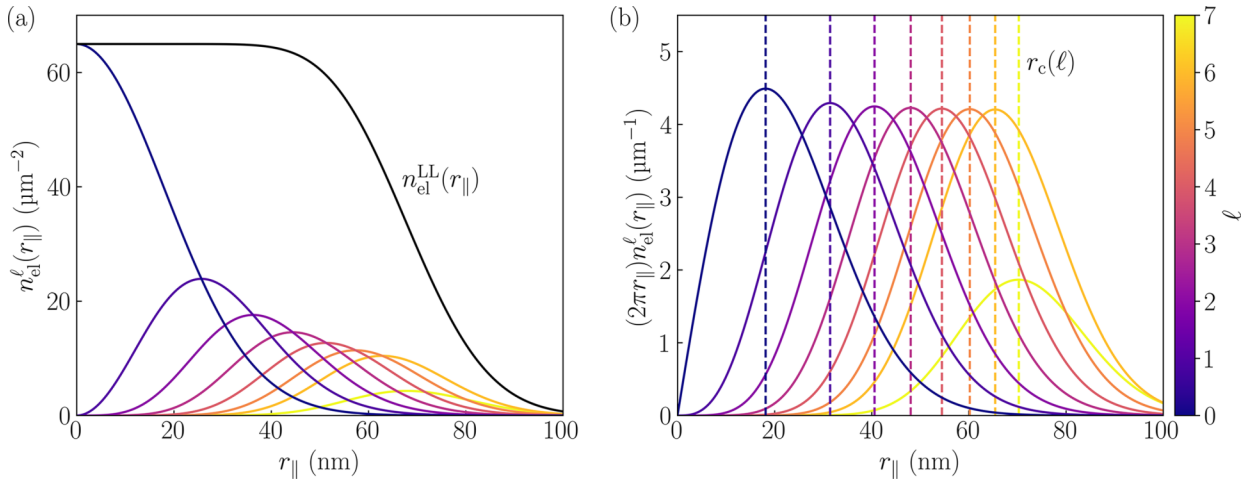


FIG. 7. (a) Energy-resolved electron density distribution $n_{\rm el}^{\ell}(r_\parallel)$ [Eq. (51)], and (b) angle-integrated energy-resolved electron density distribution $(2\pi r_\parallel)n_{\rm el}^{\ell}(r_\parallel)$ as a function of the radius $r_\parallel$ for the energy quantum numbers from $\ell = 0$ to $\ell = 7$. The black line in (a) represents $n_{\rm el}^{\rm LL}(r_\parallel)$ [Eq. (49)], and the dashed lines in (b) indicate the Larmor radius $r_{\rm c}(\ell)$ [Eq. (1)], where $(2\pi r_\parallel)n_{\rm el}^{\ell}(r_\parallel)$ is maximal. All parameters are listed in Table I.

magnetic field ($B = 0$), i.e., scattering from the disk-shaped sample $S_{\rm D}(r; q_\parallel)$.

While we expect the separation into a geometry-dependent diffraction envelope $S_{\rm D}(r; q_\parallel)$ and the LL scattering spectrum $S_{\rm LL}(q_\parallel, B)$ to be generic, the present theory cannot provide quantitative optimization criteria for sample shapes, as it is developed for a circular geometry. However, complex geometries introduce additional edge-related perturbations of the cyclotron motion [42,43], such that simple sample geometries are indeed advantageous. To further avoid perturbations of the cyclotron orbits, the $B = 0$ mean-free path should exceed the magnetic length l_B, pointing towards high-mobility GaAs quantum wells and low temperatures [44,45]. At the same time, a vanishing $B = 0$ reference signal over the relevant $q_\parallel$ range would make the isolation of the LL scattering spectrum $S_{\rm LL}(q_\parallel, B)$ by division impractical. Though disorder is beyond the scope of the present model, we note that structural disorder [10,46–48] on length scales exceeding l_B might enhance the signal-to-noise ratio of the LL scattering spectrum, which constitutes an interesting direction for future research.

The LL scattering spectrum $S_{\rm LL}(q_\parallel, B)$ reflects elastic scattering by Landau orbits: the corresponding spatially resolved LL electron density distribution $n_{\rm el}^{\rm LL}(r_\parallel)$ reveals the internal structure of the Landau-quantized electrons. The width of $n_{\rm el}^{\rm LL}(r_\parallel)$ resembles the Larmor radius $r_{\rm c}(\ell_F)$ of the highest occupied LL and decreases with increasing magnetic field. A projection onto Laguerre polynomials enables the reconstruction of individual Landau orbits, i.e., energy-resolved ring-shaped electron densities $n_{\rm el}^{\ell}(r_\parallel)$, proportional to the probability density $|\varphi_{\ell,m=0}(\mathbf{r}_\parallel)|^2$, with a maximum at the respective Larmor radius $r_{\rm c}(\ell) = l_B\sqrt{2\ell+1}$.

ACKNOWLEDGMENTS

We thank Andrei Benediktovitch and Nina Rohringer (Deutsches Elektronen-Synchrotron, Hamburg) for valuable discussions and comments on the manuscript. The authors acknowledge financial support from the Deutsche Forschungsgemeinschaft (DFG) through Projects No. 556436549 (S.M.), No. 527838492 (J.S.), and No. 420760124 (A.K.). A.K. was supported by the "Stephenson Distinguished Visitor Programme" at DESY in Hamburg (Germany). S.H. acknowledges financial support from the Natural Sciences and Engineering Research Council of Canada (NSERC) and the Alexander von Humboldt Foundation through a Humboldt Award. L.G. received support from the Alexander von Humboldt Foundation through a Feodor Lynen Research Fellowship. Further, we acknowledge the assistance of generative AI (ChatGPT and Microsoft Copilot) in improving the language clarity of this manuscript.

DATA AVAILABILITY

The data that support the findings of this article are openly available [50].

APPENDIX A: FOURIER TRANSFORM DEFINITIONS

The Fourier transform regarding the in-plane spatial coordinates $\mathbf{r}_\parallel = (x, y)^T$ and its inverse for an arbitrary scalar or vector function $\mathbf{f}$ are given by

$$\mathbf{f}(\mathbf{r}) = \frac{1}{(2\pi)^2}\int \mathrm{d}^2 q_\parallel\, e^{i\mathbf{q}_\parallel\cdot\mathbf{r}_\parallel}\mathbf{f}(\mathbf{q}_\parallel, z), \tag{A1}$$

$$\mathbf{f}(\mathbf{q}_\parallel, z) = \int \mathrm{d}^2 r_\parallel\, e^{-i\mathbf{q}_\parallel\cdot\mathbf{r}_\parallel}\mathbf{f}(\mathbf{r}). \tag{A2}$$

The Fourier transform with respect to time is defined with opposite sign in the exponential compared to the spatial transformation:

$$f(t) = \frac{1}{2\pi}\int \mathrm{d}\omega\, f(\omega)e^{-i\omega t}, \tag{A3}$$

$$f(\omega) = \int \mathrm{d}t\, f(t)e^{i\omega t}. \tag{A4}$$

APPENDIX B: ELECTRIC FIELD AT THE DETECTOR

In Eq. (15) of the main text the scattered electric field is given in frequency space:

$$\hat{\mathbf{E}}^{(+)}(\mathbf{r}, \omega) = \frac{i\omega\mu_0}{4\pi}\frac{e^{ikr}}{r}\int \mathrm{d}^3 r'\, \hat{\mathbf{j}}_\perp^{(+)}(\mathbf{r}', \omega)e^{-i\mathbf{k}\cdot\mathbf{r}'}. \tag{B1}$$

In this appendix we determine the scattered electric field at the detector in time domain. A Fourier transform yields

$$\hat{\mathbf{E}}^{(+)}(\mathbf{r},t) = -\frac{\partial}{\partial t}\left[\frac{\mu_0}{4\pi r}\int \mathrm{d}^3r'\,\hat{\mathbf{j}}_\perp^{(+)}\left(\mathbf{r}', t - \frac{r - \mathbf{e}_\mathbf{r}\cdot\mathbf{r}'}{c}\right)\right], \tag{B2}$$

where we inserted $\mathbf{k} = \frac{\omega}{c}\mathbf{e}_\mathbf{r}$ or $k = \omega/c$. In the rotating frame,

$$\hat{\mathbf{j}}_\perp^{(+)}(\mathbf{r},t) = \hat{\tilde{\mathbf{j}}}_\perp^{(+)}(\mathbf{r},t)e^{-i\omega_0 t}, \tag{B3}$$

and if we apply the slowly varying envelope approximation, we obtain

$$\hat{\mathbf{E}}^{(+)}(\mathbf{r},t) \approx \frac{i\omega_0\mu_0}{4\pi r}\int \mathrm{d}^3r'\,\hat{\tilde{\mathbf{j}}}_\perp^{(+)}\left(\mathbf{r}', t - \frac{\mathbf{r} - \mathbf{e}_\mathbf{r}\cdot\mathbf{r}'}{c}\right) \times e^{-i\omega_0(t-\frac{r-\mathbf{e}_\mathbf{r}\cdot\mathbf{r}'}{c})}. \tag{B4}$$

Neglecting the retardation time in the slowly varying quantity $\hat{\tilde{\mathbf{j}}}_\perp^{(+)}$ and approximating $\mathbf{k} \approx \frac{\omega_0}{c}\mathbf{e}_\mathbf{r}$ yields

$$\begin{aligned}\hat{\mathbf{E}}^{(+)}(\mathbf{r},t) &\approx \frac{i\omega_0\mu_0}{4\pi r}e^{i\omega_0 r/c}\int \mathrm{d}^3r'\,\hat{\tilde{\mathbf{j}}}_\perp^{(+)}(\mathbf{r}',t)e^{-i\omega_0 t}e^{-i\mathbf{k}\cdot\mathbf{r}'} \\ &= \frac{i\omega_0\mu_0}{4\pi r}e^{i\omega_0 r/c}\int \mathrm{d}^3r'\,\hat{\mathbf{j}}_\perp^{(+)}(\mathbf{r}',t)e^{-i\mathbf{k}\cdot\mathbf{r}'}.\end{aligned} \tag{B5}$$

Combining Eqs. (13), (14), and (B5) yields the scattered electric field at the detector:

$$\hat{\mathbf{E}}^{(+)}(\mathbf{r},t) = -\frac{i\omega_0\mu_0 e^2}{4\pi m^* r}e^{i\omega_0 r/c}\sum_{j_1 j_2}\int \mathrm{d}^3r'\,\psi_{j_1}^*(\mathbf{r}') \times \mathbf{A}_0^\perp\psi_{j_2}(\mathbf{r}')a_{j_1}^\dagger a_{j_2}e^{-i(\mathbf{k}-\mathbf{k}_0)\cdot\mathbf{r}'-i\omega_0 t}. \tag{B6}$$

APPENDIX C: DERIVATION OF THE STEADY-STATE SPECTRUM

In the main text, we derived the steady-state limit of the stationary scattered spectrum, Eq. (20):

$$S(\mathbf{r};\omega_\Gamma) = \int_0^\infty \mathrm{d}\tau\, e^{-i\omega_\Gamma\tau}e^{-\Gamma\tau}G(\mathbf{r};\tau) + \text{c.c.}, \tag{C1}$$

with the steady-state field correlation function

$$\lim_{t\to\infty} G(\mathbf{r};t-t',t-t'') = G(\mathbf{r};t''-t'). \tag{C2}$$

This appendix provides the derivation of Eq. (27) starting from Eq. (C1).

1. Field correlation function

First, we consider the field correlation function, Eq. (22):

$$G(\mathbf{r};t+\tau,t) = \sum_{\substack{j_1 j_2\\ j_3 j_4}}\langle a_{j_1}^\dagger(t+\tau)a_{j_2}(t+\tau)a_{j_3}^\dagger(t)a_{j_4}(t)\rangle \times \mathcal{S}_{j_1 j_2 j_3 j_4}(\mathbf{k}-\mathbf{k}_0)\left(\frac{\omega_0 r_0}{r}\right)^2|\mathbf{A}_0^\perp|^2 e^{i\omega_0\tau}, \tag{C3}$$

which depends on

$$\langle a_{j_1}^\dagger(t+\tau)a_{j_2}(t+\tau)a_{j_3}^\dagger(t)a_{j_4}(t)\rangle. \tag{C4}$$

In order to determine this correlation, we assume the LL operator dynamics to be dominated by their intrinsic time dependency,

$$a_j(t) = a_j e^{-i\omega_j t}. \tag{C5}$$

If we were to include the dynamics driven by $\mathbf{A}_0(\mathbf{r},t)$, higher-order contributions of at least $\mathcal{O}(\mathbf{A}_0^4)$ would appear in the electric field correlation [Eq. (C3)]. Rearranging to normal ordering using the commutation relations yields

$$\begin{aligned}&\langle a_{j_1}^\dagger(t+\tau)a_{j_2}(t+\tau)a_{j_3}^\dagger(t)a_{j_4}(t)\rangle \\ &\quad= \langle a_{j_1}^\dagger a_{j_3}^\dagger a_{j_4}a_{j_2}\rangle e^{i(\omega_{j_1}-\omega_{j_2}+\omega_{j_3}-\omega_{j_4})t}e^{i(\omega_{j_1}-\omega_{j_2})\tau} \\ &\qquad+ \delta_{j_2,j_3}\langle a_{j_1}^\dagger a_{j_4}\rangle e^{i(\omega_{j_1}-\omega_{j_2}+\omega_{j_3}-\omega_{j_4})t}e^{i(\omega_{j_1}-\omega_{j_2})\tau}.\end{aligned} \tag{C6}$$

Within a Hartree-Fock approximation, we find

$$\begin{aligned}&\langle a_{j_1}^\dagger(t+\tau)a_{j_2}(t+\tau)a_{j_3}^\dagger(t)a_{j_4}(t)\rangle \\ &\quad\approx (\langle a_{j_1}^\dagger a_{j_2}\rangle\langle a_{j_3}^\dagger a_{j_4}\rangle - \langle a_{j_1}^\dagger a_{j_4}\rangle\langle a_{j_3}^\dagger a_{j_2}\rangle \\ &\qquad+ \delta_{j_2,j_3}\langle a_{j_1}^\dagger a_{j_4}\rangle)e^{i(\omega_{j_1}-\omega_{j_2}+\omega_{j_3}-\omega_{j_4})t}e^{i(\omega_{j_1}-\omega_{j_2})\tau}.\end{aligned} \tag{C7}$$

When we neglect transitions,

$$\langle a_{j_1}^\dagger a_{j_2}\rangle \approx \delta_{j_1,j_2}\langle a_{j_1}^\dagger a_{j_1}\rangle = \delta_{j_1,j_2}f_{j_1}, \tag{C8}$$

and only consider occupations $f_j = \langle a_j^\dagger a_j\rangle$, Eq. (C7) simplifies to

$$\begin{aligned}&\langle a_{j_1}^\dagger(t+\tau)a_{j_2}(t+\tau)a_{j_3}^\dagger(t)a_{j_4}(t)\rangle \\ &\quad\approx \delta_{j_1,j_2}\delta_{j_3,j_4}f_{j_1}f_{j_3} + e^{i(\omega_{j_1}-\omega_{j_2})\tau}\delta_{j_1,j_4}\delta_{j_2,j_3}f_{j_1}(1-f_{j_3}).\end{aligned} \tag{C9}$$

Inserting Eq. (C9) into the correlation function [Eq. (C3)] yields

$$\begin{aligned}G(\mathbf{r};\tau) &= \lim_{t\to\infty}G(\mathbf{r};t+\tau,t) \\ &= G(\mathbf{r};t+\tau,t) \\ &= \left(\frac{\omega_0 r_0}{r}\right)^2|\mathbf{A}_0^\perp|^2 e^{i\omega_0\tau}\sum_{j_1 j_2}(f_{j_1}f_{j_2}\mathcal{S}_{j_1 j_1 j_2 j_2}(\mathbf{q}) \\ &\quad+ e^{i(\omega_{j_1}-\omega_{j_2})\tau}f_{j_1}(1-f_{j_2})\mathcal{S}_{j_1 j_2 j_2 j_1}(\mathbf{q})).\end{aligned} \tag{C10}$$

2. Scattering matrix

The steady-state spectrum [Eq. (C1)] furthermore depends on the scattering matrix defined in Eq. (23):

$$\mathcal{S}_{j_1 j_2 j_3 j_4}(\mathbf{q}) = \int \mathrm{d}^3r'\,\psi_{j_1}^*(\mathbf{r}')\psi_{j_2}(\mathbf{r}')e^{i\mathbf{q}\cdot\mathbf{r}'} \times \int \mathrm{d}^3r''\,\psi_{j_3}^*(\mathbf{r}'')\psi_{j_4}(\mathbf{r}'')e^{-i\mathbf{q}\cdot\mathbf{r}''}. \tag{C11}$$

The goal of this appendix is to find a simplified equation for the scattering matrix that only depends on the in-plane position vectors $\mathbf{R}_\parallel$ of the unit cells.

Inserting the separation ansatz for the wave function [Eq. (12)] into Eq. (C11) yields

$$\mathcal{S}_{j_1 j_2 j_3 j_4}(\mathbf{q}) = \left(\int \mathrm{d}^3 r' \, \varphi^*_{j_1}(\mathbf{r}'_\parallel)\xi^*(z')u_0^*(\mathbf{r}') \times \varphi_{j_2}(\mathbf{r}'_\parallel)\xi(z')u_0(\mathbf{r}')e^{i\mathbf{q}\cdot\mathbf{r}'} \right) \times \left(\int \mathrm{d}^3 r'' \, \varphi^*_{j_3}(\mathbf{r}''_\parallel)\xi^*(z'')u_0^*(\mathbf{r}'') \times \varphi_{j_4}(\mathbf{r}''_\parallel)\xi(z'')u_0(\mathbf{r}'')e^{-i\mathbf{q}\cdot\mathbf{r}''} \right), \tag{C12}$$

where $u_0(\mathbf{r})$ is a lattice periodic Bloch function that we omitted previously in the effective mass approximation. We separate the integrals into a sum over all lattice vectors $\mathbf{R}$ and an integral over a unit cell of volume V_{UC}. The sum over all lattice vectors is then transformed into an integral. In accordance with the effective mass approximation, we assume the LL wave function as well as the confinement function to be slowly varying envelope functions that are approximately constant over the extent of a crystal unit cell. Utilizing the lattice periodicity of $u_0(\mathbf{r})$ and assuming $e^{\pm i\mathbf{q}\cdot\mathbf{r}}$ to be approximately constant within a unit cell and $e^{\pm i\mathbf{q}\cdot\mathbf{e}_z Z}$ to be constant within the quantum well, we obtain the scattering matrix in Dirac notation:

$$\mathcal{S}_{j_1 j_2 j_3 j_4}(\mathbf{q}_\parallel) = \left(\int \mathrm{d}^2 R'_\parallel \, \varphi^*_{j_1}(\mathbf{R}'_\parallel)\varphi_{j_2}(\mathbf{R}'_\parallel)e^{i\mathbf{q}_\parallel\cdot\mathbf{R}'_\parallel} \right) \times \left(\int \mathrm{d}^2 R''_\parallel \, \varphi^*_{j_3}(\mathbf{R}''_\parallel)\varphi_{j_4}(\mathbf{R}''_\parallel)e^{-i\mathbf{q}_\parallel\cdot\mathbf{R}''_\parallel} \right) = \langle\varphi_{j_1}|e^{i\mathbf{q}_\parallel\cdot\mathbf{R}_\parallel}|\varphi_{j_2}\rangle\langle\varphi_{j_3}|e^{-i\mathbf{q}_\parallel\cdot\mathbf{R}_\parallel}|\varphi_{j_4}\rangle, \tag{C13}$$

with the in-plane component of the scattering vector $\mathbf{q}_\parallel$. Due to our approximations, the only spatial dependence is on the in-plane position vector $\mathbf{R}_\parallel$ of the unit cell, which we rename into $\mathbf{r}_\parallel$ in the main text, Eq. (26).

3. Inserting the correlation function into the steady-state spectrum

In the previous subsections, we derived the correlation function (see Appendix C 1),

$$G(\mathbf{r}; t+\tau, t) = \left(\frac{\omega_0 r_0}{r}\right)^2 \left|\mathbf{A}_0^\perp\right|^2 e^{i\omega_0\tau} \sum_{j_1 j_2} (f_{j_1} f_{j_2} \mathcal{S}_{j_1 j_1 j_2 j_2}(\mathbf{q}_\parallel) + e^{i(\omega_{j_1}-\omega_{j_2})\tau} f_{j_1}(1-f_{j_2})\mathcal{S}_{j_1 j_2 j_2 j_1}(\mathbf{q}_\parallel)), \tag{C14}$$

which depends on the scattering matrix (see Appendix C 2),

$$\mathcal{S}_{j_1 j_2 j_3 j_4}(\mathbf{q}_\parallel) = \langle\varphi_{j_1}|e^{i\mathbf{q}_\parallel\cdot\mathbf{R}_\parallel}|\varphi_{j_2}\rangle\langle\varphi_{j_3}|e^{-i\mathbf{q}_\parallel\cdot\mathbf{R}_\parallel}|\varphi_{j_4}\rangle. \tag{C15}$$

This allows us to determine the steady-state spectrum [Eq. (C1)],

$$S(\mathbf{r};\omega_\Gamma) = \int_0^\infty \mathrm{d}\tau \, e^{-i\omega_\Gamma\tau} e^{-\Gamma\tau} G(\mathbf{r}; t+\tau, t) + \mathrm{c.c.}, \tag{C16}$$

by inserting Eqs. (C14) and (C15),

$$S(\mathbf{r};\omega_\Gamma,\mathbf{q}_\parallel) = \left(\frac{\omega_0 r_0}{r}\right)^2 |\mathbf{A}_0^\perp|^2 \int_0^\infty \mathrm{d}\tau \left\{ e^{-i(\omega_\Gamma-\omega_0)\tau} e^{-\Gamma\tau} \sum_{j_1 j_2} (f_{j_1} f_{j_2} \langle\varphi_{j_1}|e^{i\mathbf{q}_\parallel\cdot\mathbf{R}_\parallel}|\varphi_{j_1}\rangle\langle\varphi_{j_2}|e^{-i\mathbf{q}_\parallel\cdot\mathbf{R}_\parallel}|\varphi_{j_2}\rangle + e^{i(\omega_{j_1}-\omega_{j_2})\tau} f_{j_1}(1-f_{j_2})|\langle\varphi_{j_1}|e^{i\mathbf{q}_\parallel\cdot\mathbf{R}_\parallel}|\varphi_{j_2}\rangle|^2) \right\} + \mathrm{c.c.}, \tag{C17}$$

where we explicitly added the dependency on $\mathbf{q}_\parallel$. We utilize

$$\int_0^\infty \mathrm{d}\tau \, e^{-i\omega\tau} e^{-\Gamma\tau} = \frac{1}{\Gamma + i\omega} \tag{C18}$$

to solve the integral:

$$S(\mathbf{r};\omega_\Gamma,\mathbf{q}_\parallel) = \left(\frac{\omega_0 r_0}{r}\right)^2 |\mathbf{A}_0^\perp|^2 \sum_{j_1 j_2} \left\{ \frac{2\Gamma f_{j_1} f_{j_2}}{\Gamma^2 + (\omega_\Gamma - \omega_0)^2} \langle\varphi_{j_1}|e^{i\mathbf{q}_\parallel\cdot\mathbf{R}_\parallel}|\varphi_{j_1}\rangle\langle\varphi_{j_2}|e^{-i\mathbf{q}_\parallel\cdot\mathbf{R}_\parallel}|\varphi_{j_2}\rangle + \frac{2\Gamma f_{j_1}(1-f_{j_2})}{\Gamma^2 + (\omega_\Gamma - \omega_0 + \omega_{j_2} - \omega_{j_1})^2} |\langle\varphi_{j_1}|e^{i\mathbf{q}_\parallel\cdot\mathbf{R}_\parallel}|\varphi_{j_2}\rangle|^2 \right\}. \tag{C19}$$

In the limit of vanishing spectral width, $\Gamma \to 0$, we identify the delta distribution [51],

$$\delta(\omega) = \lim_{\Gamma\to 0} \frac{1}{\pi} \frac{\Gamma}{\Gamma^2 + \omega^2}, \tag{C20}$$

and obtain the measured spectrum:

$$S(\mathbf{r};\omega_\Gamma,\mathbf{q}_\parallel) = 2\pi \left(\tfrac{\omega_0 r_0}{r}\right)^2 |\mathbf{A}_0^\perp|^2 \textstyle\sum_{j_1 j_2} \{\delta(\omega_\Gamma - \omega_0) f_{j_1} f_{j_2} \mathcal{S}_{j_1 j_1 j_2 j_2}(\mathbf{q}_\parallel) + \delta(\omega_\Gamma - \omega_0 + \omega_{j_2} - \omega_{j_1}) f_{j_1}(1-f_{j_2})\mathcal{S}_{j_1 j_2 j_2 j_1}(\mathbf{q}_\parallel)\}. \tag{C21}$$

APPENDIX D: ELASTIC SCATTERING

In the main text we derived the steady-state spectrum for elastic scattering [Eq. (34)]:

$$S(r;\mathbf{q}_\parallel) = 2\pi\left(\frac{\omega_0 r_0}{r}\right)^2 |\mathbf{A}_0^\perp|^2 \sum_{j_1 j_2} f_{j_1} f_{j_2} \mathcal{S}_{j_1 j_1 j_2 j_2}(\mathbf{q}_\parallel). \quad \text{(D1)}$$

This appendix provides the determination of the elastic-scattering matrix $S_{j_1 j_1 j_2 j_2}(\mathbf{q}_\parallel)$, Eq. (C15), and hence an explicit equation for $S(r;\mathbf{q}_\parallel)$ [Eq. (D1)]. First, we are interested in the matrix element

$$\langle\varphi_j|e^{i\mathbf{q}_\parallel\cdot\mathbf{R}_\parallel}|\varphi_j\rangle = \langle\varphi_{\ell,m}|e^{i(q_x x+q_y y)}|\varphi_{\ell,m}\rangle. \quad \text{(D2)}$$

Within this expression, we have to treat $\mathbf{R}_\parallel$ as an operator. We rewrite the position $\mathbf{R}_\parallel$ in the exponent in terms of LL ladder operators $(a^{(\dagger)}, b^{(\dagger)})$:

$$\mathbf{R}_\parallel = \begin{pmatrix} x \\ y \end{pmatrix} = \frac{l_B}{\sqrt{2}}\begin{pmatrix} i(a-a^\dagger)+(b+b^\dagger) \\ -(a+a^\dagger)-i(b-b^\dagger). \end{pmatrix}. \quad \text{(D3)}$$

Since $[x, y] = 0$ as well as $[a^{(\dagger)}, b^{(\dagger)}] = 0$ are fulfilled, we may apply the Baker-Campbell-Hausdorff formula to directly separate the sum in the exponent into a product of exponentials:

$$\begin{aligned} e^{i\mathbf{q}_\parallel\cdot\mathbf{R}_\parallel} &= e^{iq_x x}e^{iq_y y} \\ &= e^{-q_x\frac{l_B}{\sqrt{2}}(a-a^\dagger)}e^{iq_x\frac{l_B}{\sqrt{2}}(b+b^\dagger)}e^{-iq_y\frac{l_B}{\sqrt{2}}(a+a^\dagger)}e^{q_y\frac{l_B}{\sqrt{2}}(b-b^\dagger)}. \end{aligned} \quad \text{(D4)}$$

To separate the remaining sums in the exponentials, we again use the Baker-Campbell-Hausdorff formula, which is allowed since

$$[a^{(\dagger)}, [a, a^\dagger]] = 0 = [b^{(\dagger)}, [b, b^\dagger]], \quad \text{(D5)}$$

with $[a, a^\dagger] = 1$ and $[b, b^\dagger] = 1$. We obtain

$$\begin{aligned} e^{-q_x\frac{l_B}{\sqrt{2}}(a-a^\dagger)} &= e^{q_x\frac{l_B}{\sqrt{2}}a^\dagger}e^{-q_x\frac{l_B}{\sqrt{2}}a}e^{-q_x^2\frac{l_B^2}{4}}, \\ e^{q_y\frac{l_B}{\sqrt{2}}(b-b^\dagger)} &= e^{-q_y\frac{l_B}{\sqrt{2}}b^\dagger}e^{q_y\frac{l_B}{\sqrt{2}}b}e^{-q_y^2\frac{l_B^2}{4}}, \\ e^{-iq_y\frac{l_B}{\sqrt{2}}(a+a^\dagger)} &= e^{-iq_y\frac{l_B}{\sqrt{2}}a^\dagger}e^{-iq_y\frac{l_B}{\sqrt{2}}a}e^{-q_y^2\frac{l_B^2}{4}}, \\ e^{iq_x\frac{l_B}{\sqrt{2}}(b+b^\dagger)} &= e^{iq_x\frac{l_B}{\sqrt{2}}b^\dagger}e^{iq_x\frac{l_B}{\sqrt{2}}b}e^{-q_x^2\frac{l_B^2}{4}}, \end{aligned} \quad \text{(D6)}$$

which yields

$$\begin{aligned} e^{i\mathbf{q}_\parallel\cdot\mathbf{R}_\parallel} &= e^{iq_x\frac{l_B}{\sqrt{2}}b^\dagger}e^{q_x\frac{l_B}{\sqrt{2}}a^\dagger}e^{-q_x\frac{l_B}{\sqrt{2}}a}e^{-iq_y\frac{l_B}{\sqrt{2}}a^\dagger}e^{iq_x\frac{l_B}{\sqrt{2}}b} \\ &\quad\times e^{-q_y\frac{l_B}{\sqrt{2}}b^\dagger}e^{-iq_y\frac{l_B}{\sqrt{2}}a}e^{q_y\frac{l_B}{\sqrt{2}}b}e^{-q_\parallel^2\frac{l_B^2}{2}}. \end{aligned} \quad \text{(D7)}$$

To bring this expression into normal order, we commute the central exponents:

$$e^{-q_x\frac{l_B}{\sqrt{2}}a}e^{-iq_y\frac{l_B}{\sqrt{2}}a^\dagger} = e^{-iq_y\frac{l_B}{\sqrt{2}}a^\dagger}e^{-q_x\frac{l_B}{\sqrt{2}}a}e^{iq_x q_y\frac{l_B^2}{2}} \quad \text{(D8)}$$

and

$$e^{iq_x\frac{l_B}{\sqrt{2}}b}e^{-q_y\frac{l_B}{\sqrt{2}}b^\dagger} = e^{-q_y\frac{l_B}{\sqrt{2}}b^\dagger}e^{iq_x\frac{l_B}{\sqrt{2}}b}e^{-iq_x q_y\frac{l_B^2}{2}}. \quad \text{(D9)}$$

We obtain

$$\begin{aligned} e^{i\mathbf{q}_\parallel\cdot\mathbf{R}_\parallel} &= e^{iq_x\frac{l_B}{\sqrt{2}}b^\dagger}e^{-q_y\frac{l_B}{\sqrt{2}}b^\dagger}e^{q_x\frac{l_B}{\sqrt{2}}a^\dagger}e^{-iq_y\frac{l_B}{\sqrt{2}}a^\dagger}e^{-q_x\frac{l_B}{\sqrt{2}}a}e^{-iq_y\frac{l_B}{\sqrt{2}}a} \\ &\quad\times e^{iq_x\frac{l_B}{\sqrt{2}}b}e^{q_y\frac{l_B}{\sqrt{2}}b}e^{-q_\parallel^2\frac{l_B^2}{2}} \\ &= e^{i(q_x+iq_y)\frac{l_B}{\sqrt{2}}b^\dagger}e^{(q_x-iq_y)\frac{l_B}{\sqrt{2}}a^\dagger}e^{-(q_x+iq_y)\frac{l_B}{\sqrt{2}}a}e^{i(q_x-iq_y)\frac{l_B}{\sqrt{2}}b} \\ &\quad\times e^{-q_\parallel^2\frac{l_B^2}{2}}. \end{aligned} \quad \text{(D10)}$$

Defining

$$q_z = q_x + iq_y \quad \text{and} \quad q_z^* = q_x - iq_y, \quad \text{(D11)}$$

yields

$$e^{i\mathbf{q}_\parallel\cdot\mathbf{R}_\parallel} = e^{iq_z\frac{l_B}{\sqrt{2}}b^\dagger}e^{q_z^*\frac{l_B}{\sqrt{2}}a^\dagger}e^{-q_z\frac{l_B}{\sqrt{2}}a}e^{iq_z^*\frac{l_B}{\sqrt{2}}b}e^{-q_\parallel^2\frac{l_B^2}{2}}. \quad \text{(D12)}$$

We can use the Taylor expansion of the exponential function,

$$e^x = \sum_{n=0}^{\infty}\frac{x^n}{n!}, \quad \text{(D13)}$$

and let the ladder operators act on the wave functions, where we abbreviate from now on

$$\langle\varphi_{\ell,m}| = \langle\ell, m| \quad \text{and} \quad |\varphi_{\ell,m}\rangle = |\ell, m\rangle. \quad \text{(D14)}$$

We expand and apply the exponentials individually, using

$$a^{\tilde{\ell}}|\ell, m\rangle = \begin{cases} \sqrt{\frac{\ell!}{(\ell-\tilde{\ell})!}}|\ell-\tilde{\ell}\rangle, & \tilde{\ell}\leqslant\ell \\ 0, & \tilde{\ell}>\ell \end{cases} \quad \text{(D15)}$$

and

$$b^{\tilde{m}}|\ell, m\rangle = \begin{cases} \sqrt{\frac{m!}{(m-\tilde{m})!}}|m-\tilde{m}\rangle, & \tilde{m}\leqslant m \\ 0, & \tilde{m}>m \end{cases}. \quad \text{(D16)}$$

This gives

$$\begin{aligned} &e^{iq_z^*\frac{l_B}{\sqrt{2}}b}|\ell, m\rangle \\ &= \sum_{\tilde{m}_2=0}^{\infty}\frac{\left(iq_z^*\frac{l_B}{\sqrt{2}}\right)^{\tilde{m}_2}}{\tilde{m}_2!}b^{\tilde{m}_2}|\ell, m\rangle \\ &= \sum_{\tilde{m}_2=0}^{m}\frac{\left(iq_z^*\frac{l_B}{\sqrt{2}}\right)^{\tilde{m}_2}}{\tilde{m}_2!}\sqrt{\frac{m!}{(m-\tilde{m}_2)!}}|\ell, m-\tilde{m}_2\rangle, \end{aligned} \quad \text{(D17)}$$

$$\begin{aligned} &e^{-q_z\frac{l_B}{\sqrt{2}}a}|\ell, m-\tilde{m}_2\rangle \\ &= \sum_{\tilde{\ell}_2=0}^{\infty}\frac{\left(-q_z\frac{l_B}{\sqrt{2}}\right)^{\tilde{\ell}_2}}{\tilde{\ell}_2!}a^{\tilde{\ell}_2}|\ell, m-\tilde{m}_2\rangle \\ &= \sum_{\tilde{\ell}_2=0}^{\ell}\frac{\left(-q_z\frac{l_B}{\sqrt{2}}\right)^{\tilde{\ell}_2}}{\tilde{\ell}_2!}\sqrt{\frac{\ell!}{(\ell-\tilde{\ell}_2)!}}|\ell-\tilde{\ell}_2, m-\tilde{m}_2\rangle, \end{aligned} \quad \text{(D18)}$$

$$\begin{aligned} &\langle\ell, m|e^{iq_z\frac{l_B}{\sqrt{2}}b^\dagger} \\ &= \sum_{\tilde{m}_1=0}^{\infty}\langle\ell, m|b^{\dagger\tilde{m}_1}\frac{\left(iq_z\frac{l_B}{\sqrt{2}}\right)^{\tilde{m}_1}}{\tilde{m}_1!} \\ &= \sum_{\tilde{m}_1=0}^{m}\langle\ell, m-\tilde{m}_1|\sqrt{\frac{m!}{(m-\tilde{m}_1)!}}\frac{\left(iq_z\frac{l_B}{\sqrt{2}}\right)^{\tilde{m}_1}}{\tilde{m}_1!}, \end{aligned} \quad \text{(D19)}$$

$$\begin{aligned}
&\langle \ell, m-\tilde{m}_1 | e^{q_z^* \frac{l_B}{\sqrt{2}} a^\dagger} \\
&= \sum_{\tilde{\ell}_1=0}^{\infty} \langle \ell, m-\tilde{m}_1 | a^{\dagger \tilde{\ell}_1} \frac{\left(q_z^* \frac{l_B}{\sqrt{2}}\right)^{\tilde{\ell}_1}}{\tilde{\ell}_1!} \\
&= \sum_{\tilde{\ell}_1=0}^{\ell} \langle \ell-\tilde{\ell}_1, m-\tilde{m}_1 | \sqrt{\frac{\ell!}{(\ell-\tilde{\ell}_1)!}} \frac{\left(q_z^* \frac{l_B}{\sqrt{2}}\right)^{\tilde{\ell}_1}}{\tilde{\ell}_1!}, \qquad \text{(D20)}
\end{aligned}$$

which yields, together with orthonormality,

$$\begin{aligned}
&\langle \ell, m | e^{i\mathbf{q}_\parallel \cdot \mathbf{R}_\parallel} | \ell, m \rangle \\
&= \sum_{\substack{\tilde{m}_1=0 \\ \tilde{m}_2=0}}^{m} \sum_{\substack{\tilde{\ell}_1=0 \\ \tilde{\ell}_2=0}}^{l} \sqrt{\frac{m!}{(m-\tilde{m}_1)!}} \frac{\left(iq_z \frac{l_B}{\sqrt{2}}\right)^{\tilde{m}_1}}{\tilde{m}_1!} \sqrt{\frac{\ell!}{(\ell-\tilde{\ell}_1)!}} \\
&\quad \times \frac{\left(q_z^* \frac{l_B}{\sqrt{2}}\right)^{\tilde{\ell}_1}}{\tilde{\ell}_1!} \frac{\left(iq_z^* \frac{l_B}{\sqrt{2}}\right)^{\tilde{m}_2}}{\tilde{m}_2!} \sqrt{\frac{m!}{(m-\tilde{m}_2)!}} \frac{\left(-q_z \frac{l_B}{\sqrt{2}}\right)^{\tilde{\ell}_2}}{\tilde{\ell}_2!} \\
&\quad \times \sqrt{\frac{\ell!}{(\ell-\tilde{\ell}_2)!}} e^{-\frac{l_B^2 q_\parallel^2}{2}} \delta_{\tilde{\ell}_1, \tilde{\ell}_2} \delta_{\tilde{m}_1, \tilde{m}_2} \\
&= e^{-\frac{l_B^2 q_\parallel^2}{2}} \sum_{\tilde{m}=0}^{m} \frac{m!}{\tilde{m}!(m-\tilde{m})!} \frac{\left(-\frac{l_B^2 q_\parallel^2}{2}\right)^{\tilde{m}}}{\tilde{m}!} \\
&\quad \times \sum_{\tilde{\ell}=0}^{l} \frac{\ell!}{\tilde{\ell}!(\ell-\tilde{\ell})!} \frac{\left(-\frac{l_B^2 q_\parallel^2}{2}\right)^{\tilde{\ell}}}{\tilde{\ell}!} \\
&= e^{-\frac{l_B^2 q_\parallel^2}{2}} L_m\left(\frac{l_B^2 q_\parallel^2}{2}\right) L_\ell\left(\frac{l_B^2 q_\parallel^2}{2}\right). \qquad \text{(D21)}
\end{aligned}$$

In the last step, we identified the Laguerre polynomial:

$$L_n(x) = \sum_{\tilde{n}=0}^{n} \binom{n}{\tilde{n}} \frac{(-1)^{\tilde{n}}}{\tilde{n}!} x^{\tilde{n}}. \qquad \text{(D22)}$$

We then obtain for the full scattering matrix element

$$\begin{aligned}
\mathcal{S}_{j_1 j_1 j_2 j_2}(\mathbf{q}_\parallel) &= \langle \varphi_{j_1} | e^{i\mathbf{q}_\parallel \cdot \mathbf{R}_\parallel} | \varphi_{j_1} \rangle \langle \varphi_{j_2} | e^{-i\mathbf{q}_\parallel \cdot \mathbf{R}_\parallel} | \varphi_{j_2} \rangle \\
&= e^{-l_B^2 q_\parallel^2} L_{m_1}\left(\frac{l_B^2 q_\parallel^2}{2}\right) L_{m_2}\left(\frac{l_B^2 q_\parallel^2}{2}\right) \\
&\quad \times L_{\ell_1}\left(\frac{l_B^2 q_\parallel^2}{2}\right) L_{\ell_2}\left(\frac{l_B^2 q_\parallel^2}{2}\right). \qquad \text{(D23)}
\end{aligned}$$

The structure of Eq. (D23) is in agreement with Refs. [13,20,52,53]. Inserting Eq. (D23) into Eq. (D1) yields

$$\begin{aligned}
S(r; q_\parallel) &= 2\pi \left(\frac{\omega_0 r_0}{r}\right)^2 |\mathbf{A}_0^\perp|^2 e^{-l_B^2 q_\parallel^2} \\
&\quad \times \left(L_{m_{\text{lim}}}\left(\frac{l_B^2 q_\parallel^2}{2}\right) \sum_{l=0}^{\infty} f_\ell L_\ell\left(\frac{l_B^2 q_\parallel^2}{2}\right) \right)^2 \\
&= 2\pi \left(\frac{\omega_0 r_0}{r}\right)^2 |\mathbf{A}_0^\perp|^2 e^{-l_B^2 q_\parallel^2} \\
&\quad \times \left(L^{(1)}_{m_{\text{lim}}}\left(\frac{l_B^2 q_\parallel^2}{2}\right) \sum_{\ell=0}^{\infty} f_\ell L_\ell\left(\frac{l_B^2 q_\parallel^2}{2}\right) \right)^2, \qquad \text{(D24)}
\end{aligned}$$

where we evaluated the Heaviside step function of the occupations [Eq. (29)], and identified the associated Laguerre polynomial [38],

$$L^{(1)}_{m_{\text{lim}}}(x) = \sum_{m=0}^{m_{\text{lim}}} L_m(x). \qquad \text{(D25)}$$

APPENDIX E: SCATTERING WITHOUT A MAGNETIC FIELD

The full elastic-scattering spectrum derived in the main text is dominated by scattering at the sample geometry (circular disk); cf. Eq. (39). Unlike scattering by LLs, disk scattering is present even without applied magnetic field. We may utilize this independency to eliminate the influence of the sample geometry by dividing the full spectrum by the spectrum without magnetic field. This appendix provides the derivation of the elastic-scattering spectrum without magnetic field.

The Drude model for the current density in a circular 2DEG of radius R in the x–y plane is

$$\mathbf{j}_{\text{D}}^{(+)}(\mathbf{r}, \omega) = \frac{\bar{n}_{\text{el}} e^2}{(-i\omega + \gamma) m^*} \mathbf{E}_0^{(+)}(\mathbf{r}, \omega) \delta(z) \Theta(R - r_\parallel), \qquad \text{(E1)}$$

with the damping rate γ. We obtain the incident optical field from the vector potential, Eq. (14),

$$\begin{aligned}
\mathbf{E}_0^{(+)}(\mathbf{r}, \omega) &= i\omega \mathbf{A}_0^{(+)}(\mathbf{r}, \omega) \\
&= 2\pi i \omega_0 \mathbf{A}_0 e^{i\mathbf{k}_0 \cdot \mathbf{r}} \delta(\omega - \omega_0). \qquad \text{(E2)}
\end{aligned}$$

We combine Eqs. (E1) and (E2) and Fourier transform into time domain:

$$\begin{aligned}
\mathbf{j}_{\text{D}}^{(+)}(\mathbf{r}, t) &= \frac{i\omega_0}{(-i\omega_0 + \gamma)} \frac{\bar{n}_{\text{el}} e^2}{m^*} \mathbf{A}_0 e^{i(\mathbf{k}_0 \cdot \mathbf{r} - i\omega_0 t)} \delta(z) \\
&\quad \times \Theta(R - r_\parallel). \qquad \text{(E3)}
\end{aligned}$$

Inserting Eq. (E3) into the electric field at the detector [Eq. (15)] yields

$$\begin{aligned}
\mathbf{E}_{\text{D}}^{(+)}(r, t) &= -\bar{n}_{\text{el}} r_0 \frac{\omega_0^2}{(-i\omega_0 + \gamma)} \frac{e^{ik_0 r}}{r} \mathbf{A}_0^\perp \\
&\quad \times \int \mathrm{d}^2 r'_\parallel \, e^{i(\mathbf{k}_0 - \mathbf{k}) \cdot \mathbf{r}'} e^{-i\omega_0 t} \Theta(R - r'_\parallel). \qquad \text{(E4)}
\end{aligned}$$

From Eqs. (18), (21), and (E4) we obtain the steady-state field correlation function without magnetic field:

$$\begin{aligned}
G_{\text{D}}(r; \tau) &= \left(\frac{\bar{n}_{\text{el}} \omega_0^2 r_0}{r}\right)^2 \frac{|\mathbf{A}_0^\perp|^2}{(\omega_0^2 + \gamma^2)} e^{i\omega_0 \tau} \\
&\quad \times \left| \int \mathrm{d}^2 r'_\parallel \, e^{i\mathbf{q}_\parallel \cdot \mathbf{r}'_\parallel} \Theta(R - r'_\parallel) \right|^2, \qquad \text{(E5)}
\end{aligned}$$

with the in-plane component of the scattering vector $\mathbf{q} = \mathbf{k} - \mathbf{k}_0$. The integral is the 2D Fourier transform of a

disk, which gives the corresponding diffracted intensity distribution [40]:

$$\left|\int \mathrm{d}^2 r'_\parallel\, e^{i\mathbf{q}_\parallel\cdot\mathbf{r}'_\parallel}\Theta(R-r'_\parallel)\right|^2 = \left|\int_0^R \mathrm{d}r'_\parallel\, r'_\parallel \int_0^{2\pi} \mathrm{d}\phi\, e^{iq_\parallel r'_\parallel\cos\phi}\right|^2$$
$$= \left|\int_0^R \mathrm{d}r'_\parallel\, 2\pi r'_\parallel J_0(q_\parallel r'_\parallel)\right|^2$$
$$= \left|\frac{2\pi R J_1(q_\parallel R)}{q_\parallel}\right|^2$$
$$= A^2\left(\frac{2J_1(q_\parallel R)}{q_\parallel R}\right)^2. \tag{E6}$$

Inserting Eqs. (E5) and (E6) into Eq. (20) and integrating over ω_Γ yields, in the limit of an ideal filter $\Gamma \to 0$, the spectrally integrated steady-state scattering spectrum without magnetic field:

$$S_\mathrm{D}(r;q_\parallel) = 2\pi(\bar{n}_\mathrm{el}A)^2\left(\frac{\omega_0^2 r_0}{r}\right)^2 \frac{|\mathbf{A}_0^\perp|^2}{(\omega_0^2+\gamma^2)} \times \left(\frac{2J_1(q_\parallel R)}{q_\parallel R}\right)^2. \tag{E7}$$

Since we did not include damping in our derivation of the full scattering spectrum in the main text, we consistently neglect damping in the Drude model, $\gamma \to 0$:

$$S_\mathrm{D}(r;q_\parallel) = 2\pi(\bar{n}_\mathrm{el}A)^2\left(\frac{\omega_0 r_0}{r}\right)^2 |\mathbf{A}_0^\perp|^2\left(\frac{2J_1(q_\parallel R)}{q_\parallel R}\right)^2$$
$$= S(r;q_\parallel=0)\left(\frac{2J_1(q_\parallel R)}{q_\parallel R}\right)^2, \tag{E8}$$

where we identified the full elastic-scattering spectrum for parallel incidence and detection [Eq. (36)].

APPENDIX F: FOURIER TRANSFORM OF $n_\mathrm{el}^\mathrm{LL}$

In Sec. III B of the main text, we derived the momentum-resolved electron density distribution without influence of the sample geometry:

$$n_\mathrm{el}^\mathrm{LL}(q_\parallel) = \frac{1}{\nu} e^{-\frac{l_B^2 q_\parallel^2}{2}} \sum_{\ell=0}^{\infty} f_\ell(B) L_\ell\left(\frac{l_B^2 q_\parallel^2}{2}\right). \tag{F1}$$

This appendix provides the Fourier transform into position space:

$$n_\mathrm{el}^\mathrm{LL}(r_\parallel) = \frac{1}{(2\pi)^2\nu}\sum_{\ell=0}^{\infty} f_\ell(B)\int \mathrm{d}^2 q_\parallel\, e^{i\mathbf{q}_\parallel\cdot\mathbf{r}_\parallel} e^{-\frac{l_B^2 q_\parallel^2}{2}} \times L_\ell\left(\frac{l_B^2 q_\parallel^2}{2}\right)$$
$$= \frac{1}{(2\pi)^2\nu}\sum_{\ell=0}^{\infty} f_\ell(B)\sum_{n=0}^{\ell}\binom{\ell}{n}\frac{(-1)^n}{n!}\left(\frac{l_B^2}{2}\right)^n \times \int \mathrm{d}^2 q_\parallel\, q_\parallel^{2n} e^{i\mathbf{q}_\parallel\cdot\mathbf{r}_\parallel} e^{-\frac{l_B^2 q_\parallel^2}{2}}$$
$$= \frac{1}{\nu}\sum_{\ell=0}^{\infty} f_\ell(B)\sum_{n=0}^{\ell}\binom{l}{n}\frac{(-1)^n}{n!}\left(\frac{l_B^2}{2}\right)^n (-i\nabla)^{2n} \times \frac{1}{(2\pi)^2}\int \mathrm{d}^2 q_\parallel\, e^{i\mathbf{q}_\parallel\cdot\mathbf{r}_\parallel} e^{-\frac{l_B^2 q_\parallel^2}{2}}, \tag{F2}$$

where we inserted the closed form of the Laguerre polynomial L_ℓ [Eq. (D22)] and utilized $-i\nabla e^{i\mathbf{q}_\parallel\cdot\mathbf{r}_\parallel} = \mathbf{q}_\parallel e^{i\mathbf{q}_\parallel\cdot\mathbf{r}_\parallel}$.

The integral in the second line yields [51]

$$\frac{1}{(2\pi)^2}\int \mathrm{d}^2 q_\parallel\, e^{i\mathbf{q}_\parallel\cdot\mathbf{r}_\parallel} e^{-\frac{l_B^2 q_\parallel^2}{2}} = \frac{1}{2\pi l_B^2} e^{-\frac{r_\parallel^2}{2l_B^2}}. \tag{F3}$$

We then insert Eq. (F3) into Eq. (F2) to obtain

$$n_\mathrm{el}^\mathrm{LL}(r_\parallel) = \frac{1}{2\pi l_B^2\nu}\sum_{\ell=0}^{\infty} f_\ell(B)\sum_{n=0}^{\ell}\binom{\ell}{n}\frac{1}{n!}\left(\frac{l_B^2}{2}\right)^n \nabla^{2n} e^{-\frac{r_\parallel^2}{2l_B^2}}. \tag{F4}$$

It can be shown with an inductive proof that

$$\nabla^{2n} e^{-\frac{r_\parallel^2}{2l_B^2}} = \left(-\frac{2}{l_B^2}\right)^n n! L_n\left(\frac{r_\parallel^2}{2l_B^2}\right) e^{-\frac{r_\parallel^2}{2l_B^2}} \tag{F5}$$

holds, such that

$$n_\mathrm{el}^\mathrm{LL}(r_\parallel) = \frac{\bar{n}_\mathrm{el}}{\nu^2}\sum_{\ell=0}^{\infty} f_\ell(B) e^{-\frac{r_\parallel^2}{2l_B^2}}\sum_{n=0}^{\ell}\binom{\ell}{n}(-1)^n L_n\left(\frac{r_\parallel^2}{2l_B^2}\right). \tag{F6}$$

We substitute $x = r_\parallel^2/(2l_B^2)$ to evaluate the sum:

$$\sum_{n=0}^{\ell}\binom{\ell}{n}(-1)^n L_n(x) = \sum_{n=0}^{\ell}\binom{\ell}{n}(-1)^n\sum_{k=0}^{n}\binom{n}{k}\frac{(-1)^k}{k!}x^k, \tag{F7}$$

where we again inserted Eq. (D22) for L_n. Since $\binom{\ell}{n}$ ensures $\ell \geqslant n$ and $\binom{n}{k}$ ensures $n \geqslant k$, we may change the limits of both

sums:

$$\sum_{n=0}^{\ell}\binom{\ell}{n}(-1)^n L_n(x) = \sum_{k=0}^{\ell}\frac{(-x)^k}{k!}\sum_{n=k}^{\ell}\binom{\ell}{n}\binom{n}{k}(-1)^n$$
$$= \sum_{k=0}^{\ell}\frac{(-x)^k}{k!}\binom{\ell}{k}\sum_{n=k}^{\ell}\binom{\ell-k}{n-k}(-1)^n. \tag{F8}$$

Substituting $j = n - k$ yields

$$\sum_{n=0}^{\ell}\binom{\ell}{n}(-1)^n L_n(x) = \sum_{k=0}^{\ell}\frac{(-x)^k}{k!}\binom{\ell}{k}\sum_{j=0}^{\ell-k}\binom{\ell-k}{j}(-1)^{j+k}$$
$$= \sum_{k=0}^{\ell}\frac{x^k}{k!}\binom{\ell}{k}\sum_{j=0}^{\ell-k}\binom{\ell-k}{j}(-1)^j 1^{\ell-k-j}$$
$$= \sum_{k=0}^{\ell}\frac{x^k}{k!}\binom{\ell}{k}\delta_{\ell,k}$$
$$= \frac{x^\ell}{\ell!}, \tag{F9}$$

where we utilized the binomial theorem to identify the Kronecker delta.

Finally, we insert Eq. (F9) into Eq. (F6):

$$n_{\mathrm{el}}^{\mathrm{LL}}(r_\parallel) = \frac{\bar{n}_{\mathrm{el}}}{\nu^2}\sum_{\ell=0}^{\infty}\frac{f_\ell(B)}{\ell!}\left(\frac{r_\parallel^2}{2l_B^2}\right)^\ell e^{-\frac{r_\parallel^2}{2l_B^2}}, \tag{F10}$$

which is similar to Ref. [10]. From a comparison with the LL wave function for $m = 0$ [cf. Eq. (9)],

$$\varphi_{\ell,m=0}(z_{\mathbb{C}}, z_{\mathbb{C}}^*) = \frac{1}{l_B\sqrt{2\pi\,\ell!}}\left(\frac{z_{\mathbb{C}}^*}{\sqrt{2}l_B}\right)^\ell e^{-\frac{|z_{\mathbb{C}}|^2}{4l_B^2}}, \tag{F11}$$

we obtain

$$n_{\mathrm{el}}^{\mathrm{LL}}(r_\parallel) = \frac{1}{\nu}\sum_{\ell=0}^{\infty} f_\ell(B)|\varphi_{\ell,m=0}(\mathbf{r}_\parallel)|^2. \tag{F12}$$

[1] T. Ando, A. B. Fowler, and F. Stern, Electronic properties of two-dimensional systems, Rev. Mod. Phys. **54**, 437 (1982).

[2] K. v. Klitzing, G. Dorda, and M. Pepper, New method for high-accuracy determination of the fine-structure constant based on quantized Hall resistance, Phys. Rev. Lett. **45**, 494 (1980).

[3] D. C. Tsui, H. L. Stormer, and A. C. Gossard, Two-dimensional magnetotransport in the extreme quantum limit, Phys. Rev. Lett. **48**, 1559 (1982).

[4] L. Schubnikow and W. J. De Haas, A new phenomenon in the change of resistance in a magnetic field of single crystals of bismuth, Nature (London) **126**, 500 (1930).

[5] D. Weiss, K. V. Klitzing, K. Ploog, and G. Weimann, Magnetoresistance oscillations in a two-dimensional electron gas induced by a submicrometer periodic potential, Europhysics Letters (EPL) **8**, 179 (1989).

[6] L. Landau, Diamagnetismus der metalle, Z. Phys. **64**, 629 (1930).

[7] M. O. Goerbig, P. Lederer, and C. M. Smith, Competition between quantum-liquid and electron-solid phases in intermediate Landau levels, Phys. Rev. B **69**, 115327 (2004).

[8] H. T. Takahashi, Landau level spectroscopy by optical angular momentum, Ph.D. thesis, Open University of Japan, 2020.

[9] O. Ciftja, Detailed solution of the problem of Landau states in a symmetric gauge, Eur. J. Phys. **41**, 035404 (2020).

[10] K. Hashimoto, T. Champel, S. Florens, C. Sohrmann, J. Wiebe, Y. Hirayama, R. A. Römer, R. Wiesendanger, and M. Morgenstern, Robust nodal structure of Landau level wave functions revealed by Fourier transform scanning tunneling spectroscopy, Phys. Rev. Lett. **109**, 116805 (2012).

[11] Bence Bernáth, P. Gogoi, A. Marchese, D. Kamenskyi, H. Engelkamp, D. Arslanov, B. Redlich, P. C. M. Christianen, and Jan C. Maan, Nonlinear terahertz transmission spectroscopy on Ga-doped germanium in high magnetic fields, Phys. Rev. B **105**, 205204 (2022).

[12] P. A. Wolff, Thomson and Raman scattering by mobile electrons in crystals, Phys. Rev. Lett. **16**, 225 (1966).

[13] A. Fainstein, T. Ruf, M. Cardona, V. I. Belitsky, and A. Cantarero, Electronic and acoustic-phonon inter-Landau-level Raman scattering in $GaAs/Al_xGa_{1-x}As$ multiple quantum wells, Phys. Rev. B **51**, 7064 (1995).

[14] H. L. Cui, V. Fessatidis, and P. Vasilopoulos, Inelastic light scattering from a modulated two-dimensional electron gas in magnetic fields, Phys. Rev. B **52**, 13765 (1995).

[15] D. X. Nguyen and D. T. Son, Probing the spin structure of the fractional quantum Hall magnetoroton with polarized Raman scattering, Phys. Rev. Res. **3**, 023040 (2021).

[16] A. Pinczuk, B. S. Dennis, L. N. Pfeiffer, K. W. West, and E. Burstein, Inelastic light scattering by the two-dimensional electron gas: Fractional quantum Hall regime and beyond, Philos. Mag. B **70**, 429 (1994).

[17] R. E. Slusher, C. K. N. Patel, and P. A. Fleury, Inelastic light scattering from Landau-level electrons in semiconductors, Phys. Rev. Lett. **18**, 77 (1967).

[18] J. Worlock, A. Pinczuk, Z. Tien, C. Perry, H. Störmer, R. Dingle, A. Gossard, W. Wiegmann, and R. Aggarwal, Spectroscopy of Landau transitions of two-dimensional electron gases, Solid State Commun. **40**, 867 (1981).

[19] T. D. Rhone, J. Yan, Y. Gallais, A. Pinczuk, L. Pfeiffer, and K. West, Rapid collapse of spin waves in nonuniform phases of the second Landau level, Phys. Rev. Lett. **106**, 196805 (2011).

[20] D. Richards, Inelastic light scattering from inter-Landau level excitations in a two-dimensional electron gas, Phys. Rev. B **61**, 7517 (2000).

[21] S. Luin, V. Pellegrini, A. Pinczuk, B. S. Dennis, L. N. Pfeiffer, and K. W. West, Resonant Rayleigh scattering from bilayer quantum Hall phases, Phys. Rev. Lett. **97**, 216802 (2006).

[22] V. Bisti, A. Zhuravlev, and L. Kulik, Resonant Rayleigh scattering by 2DES in high magnetic field, Physica B **460**, 245 (2015).

[23] R. Z. Vitlina, L. I. Magarill, and A. V. Chaplik, Light scattering by a 2D electron system with spin-orbit interaction in a strong magnetic field, J. Exp. Theor. Phys. **117**, 1131 (2013).
[24] L. V. Kulik, K. Ovchinnikov, A. S. Zhuravlev, V. E. Bisti, I. V. Kukushkin, S. Schmult, and W. Dietsche, Resonant Rayleigh scattering as a probe of spin polarization in a two-dimensional electron system, Phys. Rev. B **85**, 113403 (2012).
[25] V. Bellani, F. Rossella, M. Amado, E. Diez, K. Kowalik, G. Biasiol, and L. Sorba, Circularly polarized resonant Rayleigh scattering and skyrmions in the $\nu = 1$ quantum Hall ferromagnet, Phys. Rev. B **83**, 193307 (2011).
[26] K. Dini, O. V. Kibis, and I. A. Shelykh, Magnetic properties of a two-dimensional electron gas strongly coupled to light, Phys. Rev. B **93**, 235411 (2016).
[27] M. Morgenstern, J. Klijn, C. Meyer, and R. Wiesendanger, Real-space observation of drift states in a two-dimensional electron system at high magnetic fields, Phys. Rev. Lett. **90**, 056804 (2003).
[28] R. Roldán, J.-N. Fuchs, and M. O. Goerbig, Spin-flip excitations, spin waves, and magnetoexcitons in graphene Landau levels at integer filling factors, Phys. Rev. B **82**, 205418 (2010).
[29] Z. F. Ezawa and G. Tsitsishvili, Quantum Hall ferromagnets, Rep. Prog. Phys. **72**, 086502 (2009).
[30] J. K. Jain, Composite fermion theory of exotic fractional quantum Hall effect, Annu. Rev. Condens. Matter Phys. **6**, 39 (2015).
[31] M. Ismail, Analytic properties of complex Hermite polynomials, Trans. Am. Math. Soc. **368**, 1189 (2016).
[32] N. Rohringer, Introduction to the theory of x-ray matter interaction, arXiv:1811.12052.
[33] J. D. Jackson, *Classical Electrodynamics*, 3rd ed. (Wiley, Hoboken, NJ, 2009).
[34] G. Dixit, O. Vendrell, and R. Santra, Imaging electronic quantum motion with light, Proc. Natl. Acad. Sci. **109**, 11636 (2012).
[35] W. Vogel and D.-G. Welsch, *Quantum Optics*, 3rd ed. (Wiley-VCH, Weinheim, 2006).
[36] M. O. Scully and M. S. Zubairy, *Quantum Optics* (Cambridge University Press, Cambridge, England, 1997).
[37] I. D. Vagner, T. Maniv, and E. Ehrenfreund, Ideally conducting phases in quasi two-dimensional conductors, Phys. Rev. Lett. **51**, 1700 (1983).
[38] K. Oldham, J. Myland, and J. Spanier, *An Atlas of Functions* (Springer US, New York, NY 2009).
[39] W. Demtröder, *Electrodynamics and Optics*, Undergraduate Lecture Notes in Physics (Springer International Publishing, Cham, 2019).
[40] A. C. Ipsen, New Bessel identities from Laguerre polynomials, arXiv:1203.5961.
[41] H. Wang, T. Zhang, and X. Zhou, Dark-field spectroscopy: Development, applications and perspectives in single nanoparticle catalysis, J. Phys.: Condens. Matter **31**, 473001 (2019).
[42] B. I. Halperin, Quantized Hall conductance, current-carrying edge states, and the existence of extended states in a two-dimensional disordered potential, Phys. Rev. B **25**, 2185 (1982).
[43] Y. Avishai, Y. Hatsugai, and M. Kohmoto, Persistent currents and edge states in a magnetic field, Phys. Rev. B **47**, 9501 (1993).
[44] S. Ahn and S. Das Sarma, Density-dependent two-dimensional optimal mobility in ultra-high-quality semiconductor quantum wells, Phys. Rev. Mater. **6**, 014603 (2022).
[45] D. Kim, S. Kim, D. Lee, S. Liang, F. Tay, M. J. Manfra, D.-S. Kim, and J. Kono, Terahertz Landau polaritons in nano-slots: Ultrastrong coupling under extreme spatial confinement, in *2023 48th International Conference on Infrared, Millimeter, and Terahertz Waves (IRMMW-THz)* (IEEE, Montreal, QC, Canada, 2023), pp. 1–2.
[46] T. Champel and S. Florens, Local density of states in disordered two-dimensional electron gases at high magnetic field, Phys. Rev. B **80**, 161311(R) (2009).
[47] T. Champel, S. Florens, and M. E. Raikh, Nonlocal correlations of the local density of states in disordered quantum Hall systems, Phys. Rev. B **83**, 125321 (2011).
[48] M. E. Raikh and T. V. Shahbazyan, Anomalous tunneling in a strong magnetic field and smooth random potential: The universal distribution of the localization lengths, Phys. Rev. B **51**, 9682 (1995).
[49] B. Krummheuer, V. M. Axt, T. Kuhn, I. D'Amico, and F. Rossi, Pure dephasing and phonon dynamics in GaAs- and GaN-based quantum dot structures: Interplay between material parameters and geometry, Phys. Rev. B **71**, 235329 (2005).
[50] S. Meyer, Dataset for: Proposal for resolving quantized Landau orbits via elastic XUV scattering, Zenodo (2026), doi:https://doi.org/10.5281/zenodo.18695029
[51] E. Zeidler (ed.), *Springer-Taschenbuch der Mathematik: Begründet von I.N. Bronstein und k.A. Semendjaew weitergeführt von G. Grosche, V. Ziegler und D. Ziegler herausgegeben von E. Zeidler* (Springer Fachmedien Wiesbaden, Wiesbaden, 2013).
[52] A. H. MacDonald, Influence of Landau-level mixing on the charge-density-wave state of a two-dimensional electron gas in a strong magnetic field, Phys. Rev. B **30**, 4392 (1984).
[53] H. C. A. Oji and A. H. MacDonald, Magnetoplasma modes of the two-dimensional electron gas at nonintegral filling factors, Phys. Rev. B **33**, 3810 (1986).